

Hot subdwarfs in close binaries observed from space I: orbital, atmospheric, and absolute parameters and the nature of their companions

V. Schaffenroth¹, I. Pelisoli^{2, 1}, B. N. Barlow³, S. Geier¹, and T. Kupfer⁴

¹ Institute for Physics and Astronomy, University of Potsdam, Karl-Liebknecht-Str. 24/25, 14476 Potsdam, Germany
e-mail: schaffenroth@astro.physik.uni-potsdam.de

² Department of Physics, University of Warwick, Gibet Hill Road, Coventry CV4 7AL, UK

³ Department of Physics and Astronomy, High Point University, High Point, NC 27268, USA

⁴ Department of Physics and Astronomy, Texas Tech University, PO Box 41051, Lubbock, TX 79409, USA

Received 08 June 2022/ Accepted 03 July 2022

ABSTRACT

Context. About a third of the hot subdwarfs of spectral type B (sdB), which are mostly core-helium burning objects on the extreme horizontal branch, are found in close binaries with cool, low-mass stellar, substellar, or white dwarf companions. They can show light variations due to different phenomena.

Aims. Many hot subdwarfs now have space-based light curves with high signal-to-noise ratio available. We used light curves from the Transiting Exoplanet Survey Satellite and the *K2* space mission to look for more sdB binaries. Their light curves can be used to study the hot subdwarf primaries and their companions and get orbital, atmospheric, and absolute parameters for those systems, when combined with other analysis methods.

Methods. By classifying the light variations and combining this with the fit of the spectral energy distribution, the distance derived by the parallaxes obtained by *Gaia* and the atmospheric parameters, mainly from the literature, we could derive the nature of the primary and secondary in 122 (75%) of the known sdB binaries and 82 newly found reflection effect systems. We derive absolute masses, radii, and luminosities for a total of 39 hot subdwarfs with cool, low-mass companions, as well 29 known and newly found sdBs with white dwarf companions.

Results. The mass distribution of hot subdwarfs with cool, low-mass stellar and substellar companions differs from those with white dwarf companions, implying they come from different populations. By comparing the period and minimum companion mass distributions, we find that the reflection effect systems all have M dwarf or brown dwarf companions, and that there seems to be several different populations of hot subdwarfs with white dwarf binaries — one with white dwarf minimum masses around $0.4 M_{\odot}$, one with longer periods and minimum companion masses up to $0.6 M_{\odot}$ and at the shortest period another with white dwarf minimum masses around $0.8 M_{\odot}$. We also derive the first orbital period distribution for hot subdwarfs with cool, low-mass stellar or substellar systems selected from light variations instead of radial velocity variations. It shows a narrower period distribution from 1.5 hours to 35 hours compared to the distribution of hot subdwarfs with white dwarfs, which ranges from 1 hour to 30 days. These period distributions can be used to constrain the previous common envelope phase.

Key words. binaries (including multiple); close; Stars: variables: general; subdwarfs; Stars: horizontal-branch; white dwarfs; Stars: low-mass; Stars: late-type; Stars: fundamental parameters

1. Introduction

Hot subdwarfs of spectral type O and B (sdO/Bs) are a mixture of different kinds of evolved stars located at or close to the bluest end of the horizontal branch, referred to as the extreme horizontal branch (EHB). Subdwarf O stars consist of many different objects including post-red giant branch and post-asymptotic giant branch stars. Most sdBs on the other hand, which are mostly found on the EHB, are core-He burning objects with very thin envelopes and masses close to the core-helium-flash mass of $0.47 M_{\odot}$ — for sdBs coming from low-mass star progenitors. A higher mass range of 0.35 – $0.65 M_{\odot}$ is possible for sdBs originating from more massive stars. A small fraction of sdBs is composed of extremely low-mass pre-white dwarfs (pre-ELM WD), which can cross the EHB on their way to the WD cooling track (Heber 2009, 2016). Significant mass-loss on the red giant branch (RGB) is necessary to form sdO/Bs, and Han et al. (2002,

2003) proposed different binary evolution channels to form such objects. Stable mass transfer leads to a composite sdB system with a K to F type companion and orbital periods of a few hundred days (Vos et al. 2018). They are double-lined binaries in the visible range showing spectral features from both the sdB and the cool companion. In the case of a larger mass ratio — above 1.2–1.5 — the mass-transfer is unstable and results in a common-envelope phase. The outcome of this poorly understood phase (Ivanova et al. 2013) is a sdB with a cool-low mass companion with a period of 0.05 day to around one day (Schaffenroth et al. 2019). Finally, after a stable mass transfer phase has passed, unstable mass-transfer can commence once the sdB's companion evolves into a red giant, leading to a short-period binary with a WD companion. He-core burning sdBs will evolve to sdOBs and sdOs after He-exhaustion in the core, before contracting onto the WD cooling track.

Most sdB binaries exhibit different kinds of variability in their light curves. Pelisoli et al. (2020) found that many of the composite sdB binaries show small amplitude variations in their light curves with periods of 0.5 d to a few days, due to spots on the companions. Subdwarf B stars with WD companions can show ellipsoidal deformation and even Doppler beaming in their light curves when the orbit is close enough and the WD massive enough (Kupfer et al. 2022, 2020a,b, 2017b). Systems with cool, low-mass companions show unique light curve variations resulting from the extreme temperature difference and small separation distance between the two stars (as small as $0.5 - 1 R_{\odot}$). The UV-bright hot subdwarf irradiates the side of the cool companion facing it, and this leads to hot and cold sides of the companion due to their being tidally locked. The irradiated face rotating in and out of view produces a quasi-sinusoidal flux variation called the reflection effect that exhibits broad minima and sharper maxima. In systems with inclination angles $\gtrsim 60 - 65^\circ$, eclipses can be observed given the right combination of stellar sizes and orbital separation. Such eclipsing sdB binaries are called HW Vir systems (e.g. Menzies & Marang 1986; Schaffenroth et al. 2019, 2021). Finally, some hot subdwarfs show variability due to short-period pulsations on the order of minutes (for sdO/B with $T_{\text{eff}} > 30000$ K) and long-period (for sdO/B with $T_{\text{eff}} < 30000$ K), low-amplitude pulsations on the order of hours (see Lynas-Gray 2021; Kupfer et al. 2019, for a summary). Some targets in binaries can even show variability due to both pulsations and binary effects (e.g. Vučković et al. 2007).

Geier et al. (2019) published a catalogue of 39 800 hot subluminous star candidates with $G < 19$ mag based on *Gaia* DR2 (Gaia Collaboration et al. 2018) colors, parallaxes, and proper motions and several ground-based, multi-band photometry surveys. They expect the majority of the candidates to be hot sdO or sdBs, followed by blue horizontal branch stars, hot post-AGB stars, and central stars of planetary nebulae (PN). The main purpose of their catalogue is to serve as a target list for current and future large-scale photometric and spectroscopic surveys.

One of those surveys is the *TESS* (Transiting Exoplanet Survey Satellite) mission (Ricker et al. 2015), which is observing over 90% of the northern and southern sky in different sectors. Each sector has a field of view of $24^\circ \times 90^\circ$ and is observed for 27 consecutive days, with a short break halfway through for data downlinking. The full frame images are downloaded every 30 min (and since sector 28, every 10 min), providing light curves of all stars in the field-of-view of 30 min (10 min) cadence. A number of pre-selected stars are downloaded every 2 min (since sector 28 some additionally also with 20s cadence). As members of the *TESS* Asteroseismic Consortium (TASC) Working Group (WG) 8 on compact pulsators with the subgroup WG8.4 on binaries, we were able to provide input target lists including bright hot subdwarfs from the hot subluminous star candidate catalogue (Geier et al. 2019), as well as with Guest Investigator programs G022141, G03221, and G04091 (PI: Brad Barlow). The majority of these targets were submitted because they either were known variable hot subdwarfs or were strong candidates for variability based off of their anomalous *Gaia* flux errors and other metrics (Barlow et al. 2022). This provides us with a few thousand space-quality light curves of hot subdwarf stars, including the few tens of light curves already obtained from *K2* (Howell et al. 2014) from different successful proposals. Consequently, we possess for the first time an expansive, high S/N data set of hot subdwarf light curves. Sahoo et al. (2020) and Baran et al. (2021b) used the 30 min cadence *TESS* light curves of observed targets from the hot subluminous star candidate catalogue (Geier et al.

Table 1: Result of our light curve search

type	number (analyzed)
new reflection effect systems	82(0)
reflection effect systems with solved orbits	20 (17)
HW Vir systems	35 (0)
HW Vir system with solved orbits	17 (17)
ellipsoidal deformation	19 (11)
Doppler beaming	16 (1)

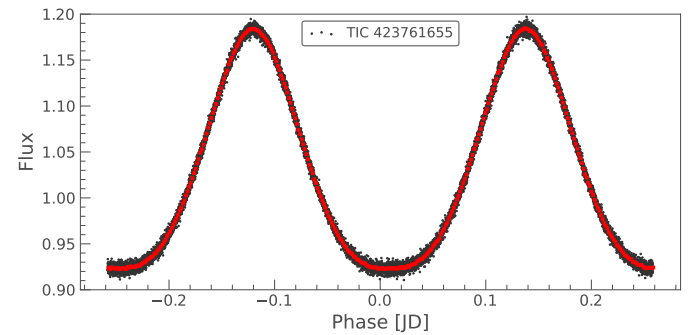


Fig. 1: Example *TESS* light curve of a reflection effect system (EC01578-1743). The light curve is shown phase-folded to the orbital period (black points) and also binned (red points).

2019) to search for light variations of hot subdwarf candidates and found several sdB+dM/BD candidates.

In this paper we present our search for hot subdwarfs with cool, low mass companions showing the reflection effect and hot subdwarfs with white dwarf companions showing ellipsoidal deformation and/or beaming, as well as a characterization of these systems. In section 2 we give more details to our target selection and our search for light variations. In section 3 we present our characterization of the primary star using the parallaxes and proper motions provided by *Gaia*, as well as the fit of the spectral energy distribution allowing us to get a mass distribution for the sdB in close binaries. In section 4 we show the distribution of the orbital parameters (period, semi-amplitude of the radial velocity curve) of our targets and compare the different populations. In section 5 we conclude and provide a short summary of our results.

2. Target selection and search for light variations

To look for reflection effect systems in the *TESS* light curves, we have searched *TESS* sectors 1-36 for variability in all stars brighter than $G < 16$ mag from the *Gaia* DR2 catalogue of hot subluminous stars (Geier et al. 2019), as well as the catalogue of spectroscopically confirmed hot subdwarf stars (in total 2883 targets with 2-min cadence light curves and 353 targets with 20-sec cadence light curves). (Geier 2020). We have used the light curves made available by the *TESS* Science Processing Operations Center (SPOC) through the Barbara A. Mikulski Archive for Space Telescopes MAST¹, using the PDCSAP flux, which corrects the simple aperture photometry (SAP) by removing instrumental trends, as well as contributions to the aperture expected to come from neighbouring stars other than the target of interest given a pre-search data conditioning (PDC). This is essential for *TESS*, as the pixel size is almost 21 arc sec. Through

¹ <https://mast.stsci.edu/>

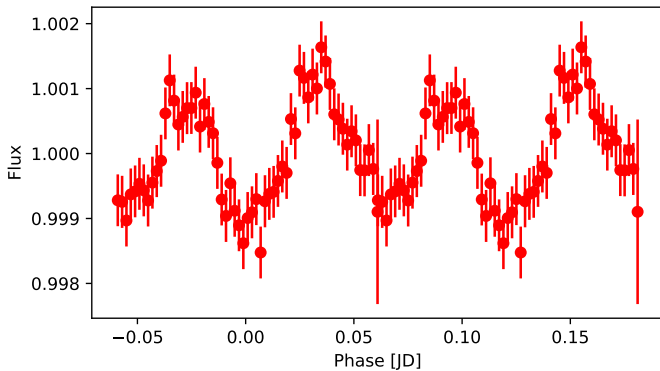


Fig. 2: Example *TESS* light curve of an ellipsoidal system (PG1043+760) showing additionally Doppler beaming. The light curve is shown phase-folded to the orbital period and binned.

the CROWDSAP parameter, the pipeline also provides an estimate of how much of the flux in the aperture belongs to the target. To avoid possible zero-point inconsistencies between different sectors, we divided the flux by the mean flux in each sector for each star.

We used the Python package Astropy (Astropy Collaboration et al. 2013, 2018) to calculate the Lomb-Scargle periodogram (Lomb 1976; Scargle 1982) of all light curves up to the Nyquist frequency, oversampling by a factor of 10. Light curves were then phase-folded to the period corresponding to the strongest peak, or twice this period for ellipsoidal systems, which have first harmonic peaks stronger than the fundamental orbital frequency. Our custom script that downloads the light curves and generates diagnostic plots with the periodogram and phase-folded light curves is publicly available². We visually inspected the diagnostic plots for all targets to confirm any variability and selected all objects showing a reflection effect (with and without eclipses), as well as stars showing ellipsoidal deformation. All targets with confirmed light variations can be found in Table A.4.

Additionally, we inspected the *TESS* or *K2* light curves of all hot subdwarfs with orbits characterized by radial velocity measurements (Kupfer et al. 2015, and references in Table A.4). All light curves were downloaded, phase-folded to the orbital period, and binned using the Python package LIGHTKURVE (Lightkurve Collaboration et al. 2018)³. We computed the periodogram around the orbital period to search for any small peaks resulting from weak reflection or ellipsoidal deformation signals. For targets without any variations, we phase-folded the light curve to the orbital period derived by time-resolved spectroscopy and determined the signal-to-noise ratio. The results of our search are shown in Table 1, A.3, and A.4. Example *TESS* light curves of a reflection effect system and an ellipsoidal system additional showing Doppler beaming can be found in Fig. 1 and 2. The complete set of light curves, along with full details regarding our modeling and analysis methods, will be presented in an additional paper (Paper II, Schaffenroth et al. in prep.).

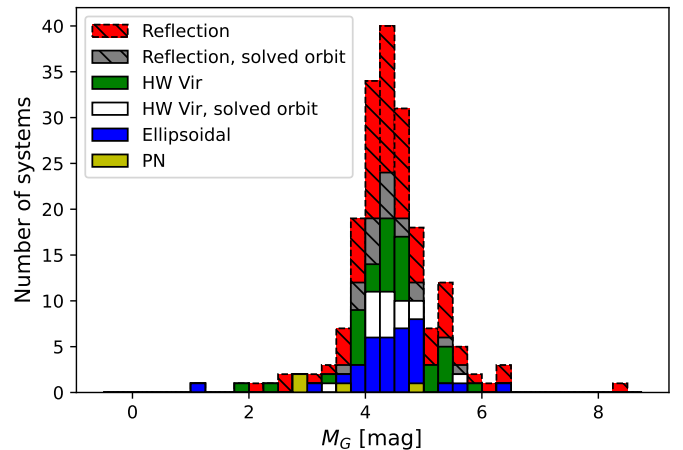


Fig. 3: *Gaia* absolute magnitude M_G of all our targets divided into different groups according to the different light curve variations they show as shown in the legend.

3. Characterizing the primary star

3.1. Absolute magnitude and reduced proper motion

3.1.1. Method

Both hot subdwarf and hot WD binaries containing a cool, low-mass companion can show a reflection effect (Schaffenroth et al. 2019), as can some sdOs that are central stars of planetary nebula (CSPN). In order to determine the true nature of the primary star, we used the colors, parallaxes, and proper motion from *Gaia* EDR3 (Gaia Collaboration et al. 2021), as was done in Schaffenroth et al. (2019) for newly discovered HW Vir systems. Using the *Gaia G* magnitude together with the parallax, we could determine the absolute magnitude of our targets using the distance modulus ($G - M_G = 5 \log_{10} d - 5$). We ensured that all of our targets but one (which we identified as a potential triple system) had a small uncertainty in their parallax ($\lesssim 10\%$) and a Renormalised Unit Weight Error (RUWE) below 1.4 (e.g., Penoyre et al. 2022). A higher RUWE indicates potential problems with the parallax.

Another way to confirm our target selection is to determine the reduced proper motions $H_G = G + 5(\log \mu + 1)$. Stars that are farther away should show less transverse velocity on average than those that are closer, and the reduced proper motion is therefore a proxy for the distance; closer objects should have larger reduced proper motions. Typically, hot subdwarfs show reduced proper motions between 5 and 14 mag (e.g. Schaffenroth et al. 2019).

3.1.2. Results

The results are found in Table A.4. Inspecting the absolute magnitude M_G distribution of all our targets (Fig. 3), we see that it peaks around $M_G = 4.5$, as expected for hot subdwarf stars (Geier 2020). We have only one target with $M_G > 7$ mag, which is most likely a WD primary. We also have some targets with $M_G < 3$ mag, which are known CSPN, or pre-ELM WD.

Our reduced proper motion distribution shown in Fig. 4 also confirms that our targets are most likely hot subdwarf stars.

Since hot subdwarfs are of spectral type O and B, they have temperatures between 25 000 to 50 000 K and blue colors. Their luminosities are lower than main sequence stars and higher than

² <https://github.com/ipelisoli/TESS-LS>

³ <https://docs.lightkurve.org>

⁴ <https://stilism.obspm.fr/>

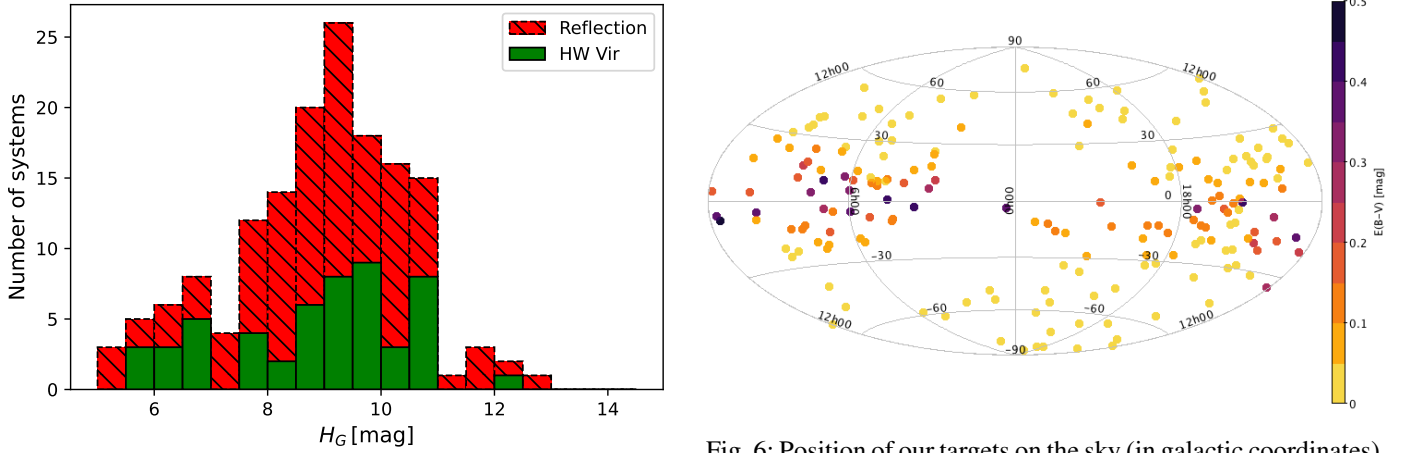


Fig. 4: Reduced proper motion of all our reflection effect systems (eclipsing and non-eclipsing).

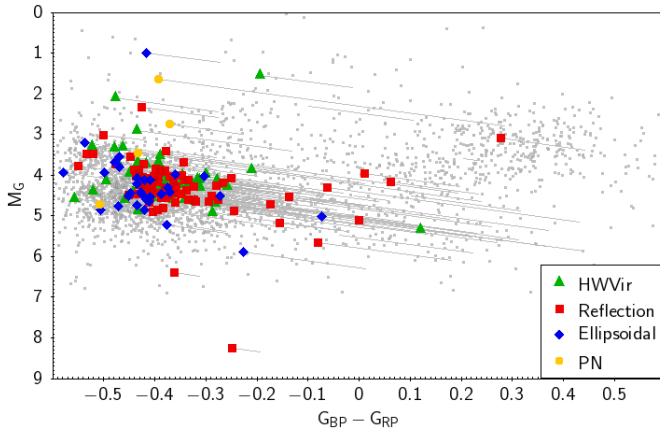


Fig. 5: $G_{\text{BP}} - G_{\text{RP}}$ vs M_G diagram. The targets are again grouped according to their light variations. All targets have been corrected for interstellar extinction using Stilism⁴. The correction is shown with the grey lines. In comparison the known sdO/Bs taken from Geier (2020) are shown with the grey data points.

hot white dwarfs. To check where we find our targets in the color-magnitude diagram, we plot a $G_{\text{BP}} - G_{\text{RP}}$ vs M_G diagram (see Fig. 5). Both the absolute magnitude and $G_{\text{BP}} - G_{\text{RP}}$ color were corrected for interstellar extinction using 3D maps (Lallemand et al. 2014; Capitanio et al. 2017). Our targets are located at $-0.5 < G_{\text{BP}} - G_{\text{RP}} < 0.3$, with most of the targets clustering at $G_{\text{BP}} - G_{\text{RP}} < -0.25$. There is a slight trend that targets with $G_{\text{BP}} - G_{\text{RP}} > -0.25$ seem to have smaller M_G . As all of those targets show a high extinction, this trend can most likely be explained by insufficient correction of the interstellar extinction. The distribution of our targets on the sky (Fig. 6) shows that most of the targets with high extinction are found close to the galactic plane, up to $\pm 20^\circ$ away. The comparison with the known sdO/Bs from Geier (2020) shows quite a good agreement. One target is found with $G_{\text{BP}} - G_{\text{RP}} = 0.3$ at an absolute magnitude $M_G = 3$, consistent with known composite sdB stars. Only a few of our targets are found at $G_{\text{BP}} - G_{\text{RP}} < -0.45$, which is probably due to the fact that most of them are cooler helium-core burning sdB stars rather than evolved sdO stars. The comparison of the position of all our targets grouped together by the observed light variations (Fig. 7) shows that all different target types seem to be equally distributed on the sky.

Fig. 6: Position of our targets on the sky (in galactic coordinates). The color coding is given by the color excess $E(B-V)$.

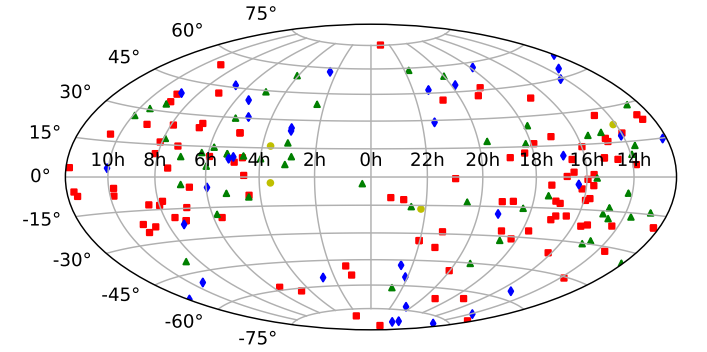


Fig. 7: Comparison of the position of our targets on the sky (in galactic coordinates). The green triangles mark HW Virs, the red squares reflection effect systems and the blue diamonds ellipsoidal systems, and the yellow circles CSPNs.

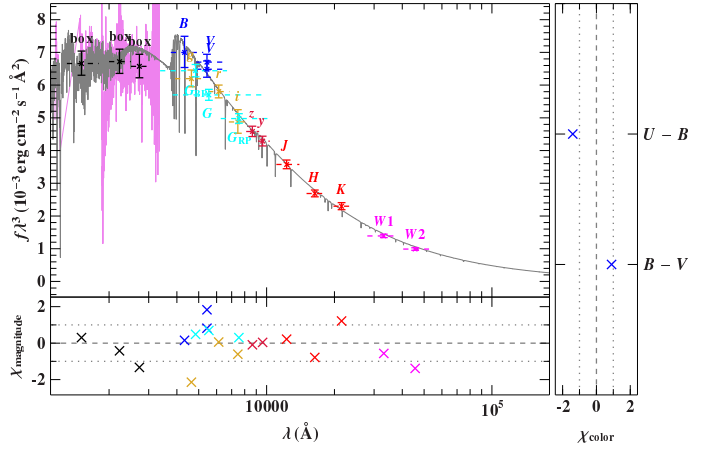


Fig. 8: Example of an SED fit (for the sdB+WD system PG1519+640).

3.2. Spectral energy distribution

3.2.1. Method

To confirm a candidate's status as a hot subdwarf, we need to derive the effective temperature T_{eff} and surface gravity $\log g$. The best way to determine atmospheric parameters is to observe and model the target's spectrum. However, it is also possible to

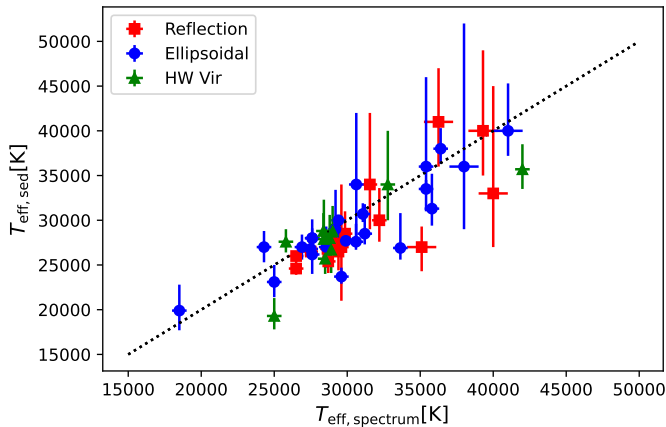


Fig. 9: Comparison of the effective temperature determined by spectral fitting and spectral energy distribution fitting. Blue circles mark systems showing ellipsoidal deformation, green triangles mark HW Vir systems and red squares mark reflection effect systems.

determine T_{eff} , as well as the radius and the luminosity, by fitting the spectral energy distribution (SED) with synthetic spectra and combining this with the distance from the *Gaia* parallax (see Heber et al. 2018; Irrgang et al. 2021, for more details on this method). The shape of the SED gives us T_{eff} as well as the interstellar reddening. And by comparing the observed and synthetic flux $f(\lambda)$ and $F(\lambda)$ respectively, we can derive the angular diameter $\theta = 0.5 \sqrt{\frac{f(\lambda)}{F(\lambda)}}$, which can be used to derive the radius $R = \theta/(2\varpi)$ and the luminosity $L/L_{\odot} = (R/R_{\odot})^2(T_{\text{eff}}/T_{\text{eff},\odot})^4$ by using the *Gaia* parallax ϖ and parallax offset.

Using the $\log g$ determined by the spectral fitting and the radius determined by the SED and *Gaia* distance, we can also derive the mass of the hot subdwarf $M = gR^2/G$ for the hot subdwarf binaries with known atmospheric parameters.

3.2.2. Results

One example SED fit is shown in Fig. 8. Unfortunately, the SED fitting is not straightforward for the reflection effect systems since our targets show light variations and the photometry we used from the literature was taken at a random phase.

In light of the above, we tested our method on reflection effect and ellipsoidal systems with known atmospheric parameters and sufficient photometric data (see Table A.1 for the results). The comparison between effective temperatures determined by spectral fitting and spectral energy distribution fitting (Fig. 9) shows that for systems with $T_{\text{eff}} \lesssim 32\,000$ K, the fitting of the SED can determine the T_{eff} very well if we neglect infrared photometry, since the contribution of the companion gets larger there. UV (IUE or Galex FUV or NUV) and SDSS u' photometry are essential for disentangling the effect of T_{eff} and interstellar reddening on the SED by covering the Balmer jump, so we exclude all targets without sufficient UV photometry from the SED fitting. For hotter systems, we see a larger scatter. For $T_{\text{eff}} > 42\,000$ K the Balmer jump is not visible anymore, and so the temperature cannot be derived anymore without constraining the interstellar reddening. There is also a slight tendency that the SED fitting derives smaller temperatures than the spectral fitting.

Using the derived luminosities, we construct a Hertzsprung-Russell diagram for reflection effect and ellipsoidal systems with

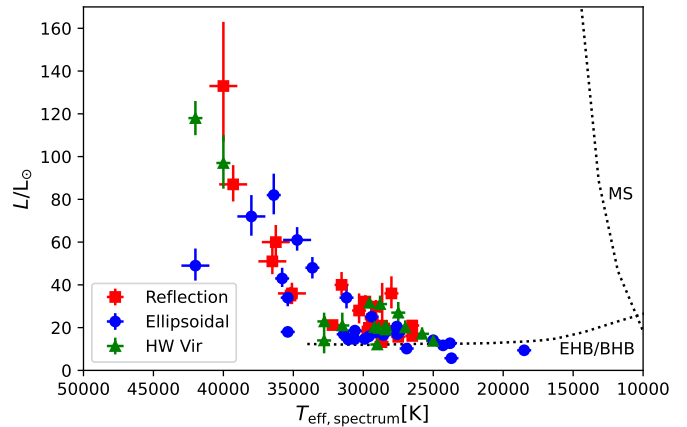


Fig. 10: Hertzsprung-Russell diagram of our targets with known atmospheric parameters. Blue circles mark systems showing ellipsoidal deformation, green triangles mark HW Vir systems and red squares mark reflection effect systems. The dotted lines mark the zero-age main sequence or EHB/BHB.

spectroscopic parameters for the first time. This is shown in Fig. 10. The sdBs on the EHB with temperatures below 33000 K are found at similar luminosities between 15 and $40 L_{\odot}$. At larger temperatures the luminosity increases with the temperature but also a larger scatter is visible resulting from larger differences in the radii. Németh et al. (2012) showed that the He abundances and the difference in He abundance increases with the temperature. The larger scatter of the radii and hence the luminosity at larger temperatures may be related to those He abundance differences.

With the spectroscopic $\log g$ and the radius from the SED fitting, we were able to derive the mass distribution of reflection effect, HW Vir and ellipsoidal systems. A similar approach was used in Krzesinski & Balona 2022, which derived the mass distribution of pulsating hot subdwarf candidates with spectroscopic parameters to be a broad peak with the maximum at $0.45 M_{\odot}$. However, they state that their analysis might not be reliable and useful to derive masses of single systems.

Our result is shown in Fig. 11, 12 and 13 and Table A.1. For the HW Vir systems, we derive a mass of $0.46^{+0.08}_{-0.12} M_{\odot}$ using a skewed normal distribution. As the typical mass error is about $0.05 M_{\odot}$ this suggests an intrinsically broader peak. The non-eclipsing reflection effect systems seem to have a broader peak with more higher-mass sdBs. As the only difference compared to the HW Vir systems is that they have no eclipses, we would not expect any difference. Determining atmospheric parameters from reflection effect systems has to be done with caution, as the contribution of the companion to the total flux changes with the orbital phase causing the reflection effect. So the atmospheric parameters have to be determined at or close to phase zero, when only the cool side of the companion is visible, or at the secondary eclipse, when the companion is occulted by the sdB in an eclipsing system. Most of the atmospheric parameters of the reflection effect systems have been determined from a single spectrum or co-added spectra at different orbital phases, causing systematic shifts to higher temperatures and higher $\log g$. This influences the determination of the radius and will result in a shifted mass. The HW Vir systems have been studied much more carefully, and so their determined atmospheric parameters are much more reliable.

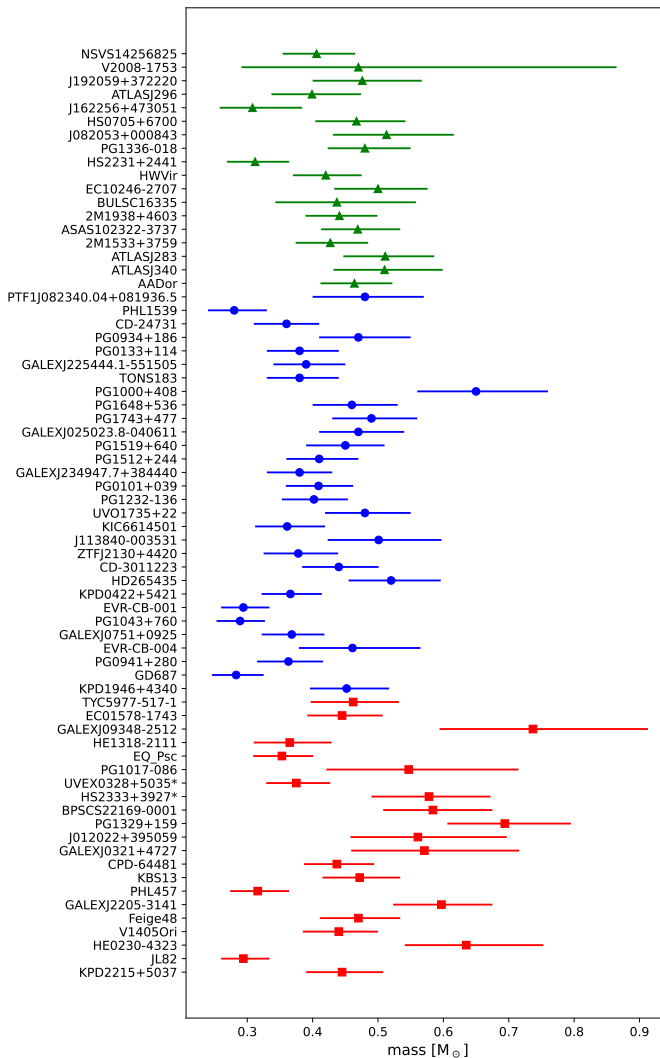


Fig. 11: Masses determined by combining the spectroscopic analysis with the fit of the SED and the *Gaia* parallaxes. Blue symbols mark systems showing ellipsoidal deformation, green symbols mark HW Vir systems and red symbols mark reflection effect systems.

The masses of the sdBs with white dwarf companions show a distribution with a similar width but a peak shifted to lower masses at $0.38^{+0.12}_{-0.08} M_{\odot}$. The distribution also seems to be slightly asymmetric, extending to higher masses. The cumulative distribution shows the shift in mass more clearly, and shows that it is indeed significant.

The samples were taken from the literature and are not complete but are suffering from selection effects, which are not easy to determine. However, in the *Gaia* color-magnitude diagram (Figure 5) and the sky distribution (Fig. 7), we can see that sdB+WD and the sdB+dM populations are overlapping well. The sdBs in the systems of both populations have been identified the same way by color selection. Hence, we expect that the selection effects should be similar for both populations and that they are comparable nevertheless.

The sdB+WD systems have been found preferably by RV variations in contrast to the HW Vir systems, as the sdB+WD systems show much smaller light variations. Both samples included only systems at the short period end of their period distribution (see Table A.4). A larger sample over a larger period

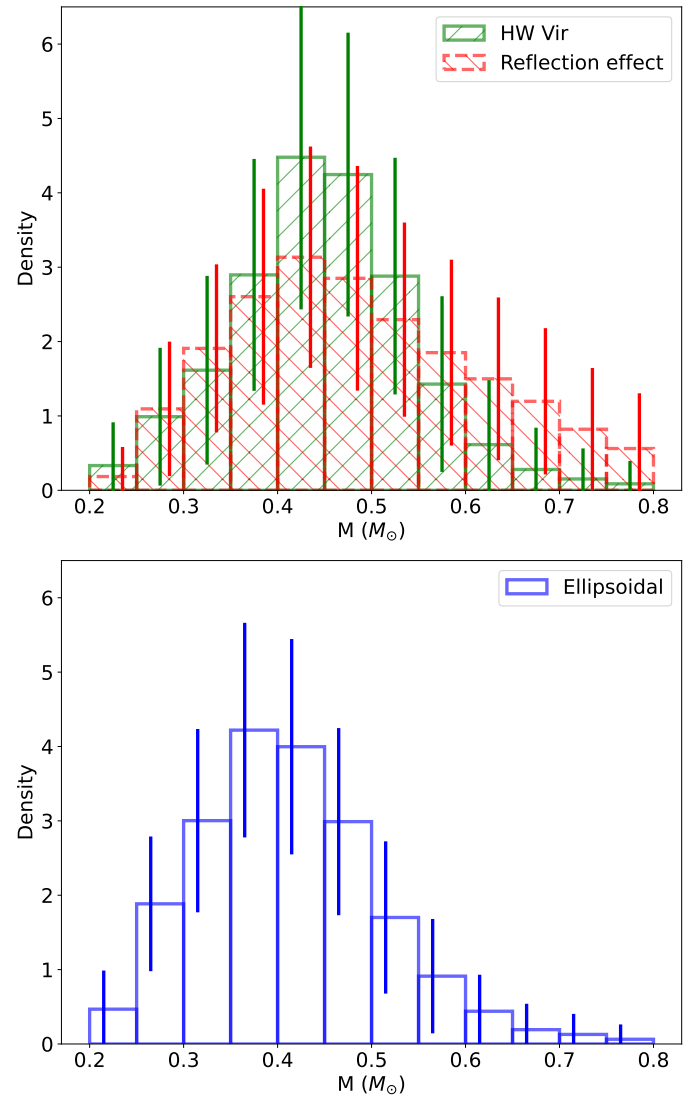


Fig. 12: Histogram of the masses determined by combining the spectroscopic analysis with the fit of the SED and the *Gaia* parallaxes.

range for both populations will be necessary to confirm our findings and also find or exclude differences of the sdB mass in systems with different orbital periods.

By fitting the SED and combining this with the *Gaia* parallax we can also constrain the atmospheric parameters of our reflection effect candidates, which do not have spectroscopic parameters, by fitting the SED and assuming a canonical mass for the sdB. From the radius we derive, we can constrain the $\log g$ in this way and constrain the atmospheric parameters for 44 targets with sufficient UV photometry. The results can be found in Table A.2. The atmospheric parameters are compared to the solved systems in the $T_{\text{eff}} - \log g$ diagram (Fig. 14). This shows that our reflection effect candidate systems are mostly found on the EHB. Some of the candidates are on post-EHB tracks, which means the He in the core was exhausted and they are evolving away from the EHB. Only one candidate was found above the EHB, which could be a lower mass pre-He WD.

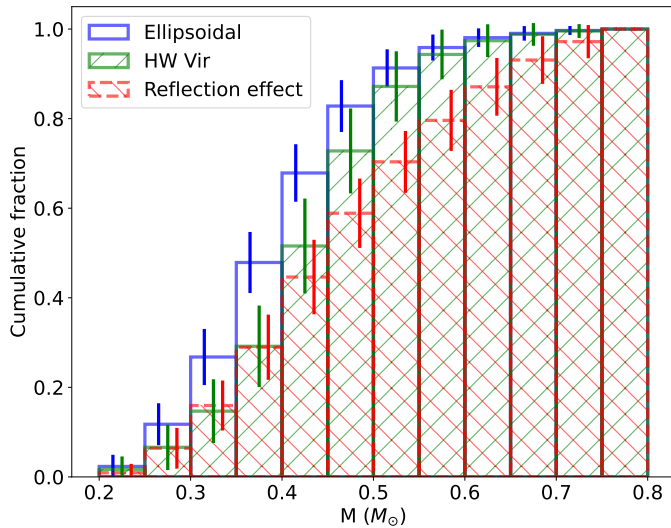


Fig. 13: Cumulative distribution of the masses determined by combining the spectroscopic analysis with the fit of the SED and the *Gaia* parallaxes.

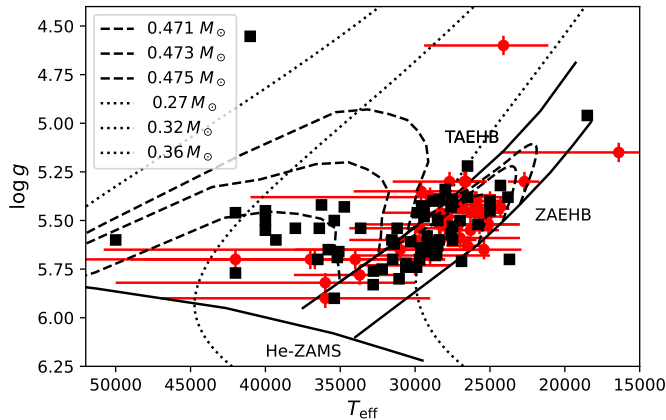


Fig. 14: T_{eff} – $\log g$ diagram of the sdB binaries with spectroscopic parameters (black squares) compared to the reflection effect candidates (red diamonds). The black solid lines mark the zero-age extreme horizontal branch (ZAEHB), the terminal-age extreme horizontal branch (TAEHB) and the He-main sequence (He-ZAMS). The dashed lines are evolutionary tracks by Dorman et al. (1993) for sdB masses of 0.471 , 0.473 , and $0.475 M_{\odot}$. The dotted lines are tracks for extremely low mass white dwarfs of a mass of 0.27 , 0.32 , and $0.36 M_{\odot}$ by Althaus et al. (2013).

4. The period distribution from light variations found by TESS

4.1. The selection effects of TESS

In order to judge the completeness of our reflection effect sample, we simulated the expected amplitude of the reflection effect for a typical sdB+dM system with different orbital periods and compared this to the noise level of the *TESS* satellite for stars of different brightness (see Fig. 15). This was done by checking the noise level in the light curves of different sdB stars of the same brightness not showing any variations in the light curve. For a 15 mag system, the detection limit is about 0.3%. As expected, the amplitude of the variations decreases with lower in-

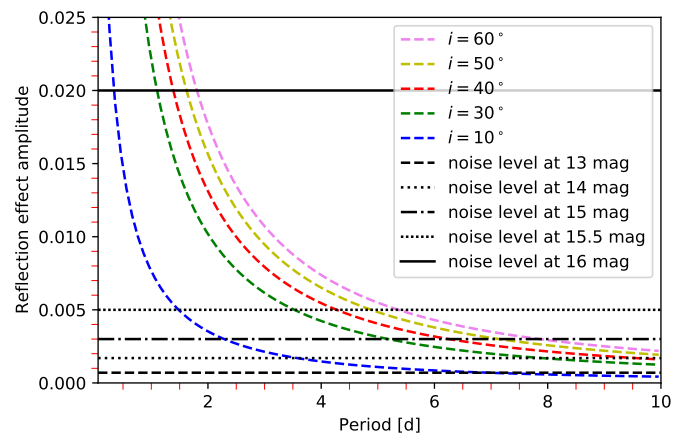


Fig. 15: Amplitude of the reflection effect of a typical sdB+dM system for different periods and inclinations. The black lines mark the *TESS* noise level for stars of different brightness.

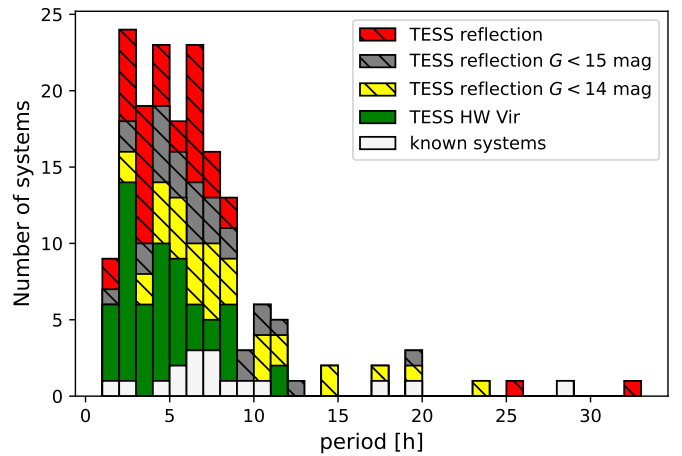


Fig. 16: Period distribution of the reflection effect systems with and without eclipses observed by *TESS*. The known reflection effect systems are marked in white, the eclipsing reflection effect systems are marked in red, and the reflection effect systems without eclipses are marked in yellow, green and grey for systems with $G < 13$ mag, $G < 14$ mag and all other systems respectively.

clination. But even with a low inclination of only 10° , we would expect to detect the reflection effect for a system brighter than 15 mag with *TESS* up to two days, for higher inclinations of about 40° up to about 6 days, and in inclinations of more than 60° up to 8 days. Since the reflection effect becomes more sinusoidal at low inclinations, it is quite hard to distinguish it from other variations like pulsations or spots. Consequently, we will probably find low-inclination reflection effects only for the systems in which the period is already known from the RV curve. But the inclination should correlate with the period, and so this should not influence the period distribution we derive.

Another selection effect could come from *TESS* having such large pixels (21 arc-sec per pixel). If another star of comparable or higher brightness is close to the star, the light curve can become contaminated. *TESS* tries to correct for this additional flux through its reported PDCSAP flux, and it uses the CROWDSAP keyword in the header to quantify the contamination level. This correction can over- or underestimate the flux, and so the am-

plitude is not entirely reliable when a bright star is so close and it contributes significantly to the flux in the target pixel. This means that we might miss some reflection effect systems when unrelated stars are too close, but overall this correction seems to be quite good (a few percent difference; see Paper II for more details) and there is no reason why this should influence the period distribution of the detected systems.

As the amplitude of the ellipsoidal modulation is much smaller as can seen in Fig. 2, this is very different for sdB+WD systems because we will only find the systems with the closest periods and/or highest mass companions by our light variation search, if the period is not known by RV variations for example.

4.2. Period distribution of the reflection effect systems

Taking all of this into account, we will never acquire a *complete* sample of reflection effect binaries from light curves alone, and the situation is even worse for the ellipsoidal systems. We do expect to find most reflection systems with higher inclinations observed by TESS up to periods around 7 days, as they can be identified from their light curve shapes with ease. Fig. 16 presents our observed orbital period distribution for sdBs with cool, low-mass companions. To ensure we do not see any difference with the brightness, we also checked the distributions of reflection effect systems of different brightness with a two-sample Kolmogorov–Smirnov test, but we could not find any significant differences. The period distribution shows that the reflection effect systems without eclipses tend to be found at periods longer than the eclipsing systems. This is expected as the eclipse probability decreases quickly with increasing separation distance and period. The period distribution shows a broad peak from 2–8 hours and falls off quickly on either end. There are very few systems with periods shorter than 2 hours, and none are below 1.2 hours. Above 8 hours, the distribution falls off quickly, and only a handful of systems are found beyond 20 hours. Despite our ability to detect systems with periods up to several days, the longest-period system we have found has a period of 35 hours. Since we do not find any longer-period systems, they either do not exist, or they are incredibly rare. As *TESS* continues to observe more and more reflection effect systems and increase the sample size, hopefully this question can be answered.

5. The companions of the close sdB binaries with solved radial velocity curves

5.1. The nature of the companion

As we have seen, the reflection effect generates a flux variation that is detectable at periods up to several days. The light variation from ellipsoidal deformation or Doppler beaming, however, is much weaker on average (below 0.1–0.2%) at periods up to about one day and not detectable at longer periods. We can use these facts to differentiate between cool, low-mass companions and white dwarf companions (more details and the analysis of those systems is shown in Paper II) for the systems with periods known from RV variations.

We phased the available light curves of all hot subdwarfs with solved orbits (135 of the 165 systems have Kepler or *TESS* light curves). Of those, 40 show a reflection effect and 33 show ellipsoidal deformation or Doppler beaming indicating that they have a white dwarf companion (see Paper II for more details). The rest do not show significant variations at the orbital period. We derived the signal-to-noise ratio for all light curves not exhibiting any variations. The result can be found in Table A.3.

To constrain the nature of the companion, we used the amplitude estimates at a given period and inclination shown in Fig. 15. Under the assumption all orbital plane orientations are equally probable, the probability of the inclination being lower than 10° is only $1 - \cos 10^\circ = 1.5\%$ (Gray 2005). Therefore, we classify as sdB+WD systems all sdB binaries with light curves having a signal-to-noise ratio smaller than the amplitude expected for a reflection effect system observed at an inclination angle $< 10^\circ$ (probability $> 98.5\%$).

Moreover, for companion masses larger than $0.45 M_\odot$ we would expect to see an infrared excess in the SED, if the companion would be a main sequence companion. Therefore, we also classify all sdB binaries with minimum companion masses $> 0.45 M_\odot$ as sdB+WD system. The minimum companion masses can be derived by the mass function

$$f(M_1, M_2) = \frac{M_2^3 \sin^3 i}{(M_1 + M_2)^2} = \frac{PK_1^3}{2\pi G}, \quad (1)$$

assuming a mass of $0.47 M_\odot$ for the sdB and an inclination of 90° . We are unable to constrain the nature of the companion in this way for only 12 of our systems, as the noise in their light curves is too large and the minimum companion mass is too small. In total, this gives us 83 sdB+WD systems and allows us to constrain the nature of 75% of all close sdB binaries with solved orbits.

Most of the sdB binaries with solved orbits have been detected by radial velocity variations, a method biased towards shorter periods, higher companion masses, and higher inclinations. Only very few of these were found by light variations. In this sample, about one-third of the sdB binaries have M dwarf or brown dwarf companions, and two-thirds have white dwarf companions.

5.2. The period distributions

The updated period distributions of the dM/BD and WD companions and their differences are also interesting, as shown in Fig. 17. We already discussed the distribution of the reflection effect and HW Vir systems showing periods from 2 hours to about 1 day. The systems with WD companions, on the other hand, show a broad distribution from just about one hour to 27 d. On top of this broad distribution we find two distinct peaks at around one day and around 5–10 days. The companion is still undefined only for a small number of systems. Most of them have periods longer than one day, agreeing well with the distribution of the WD companions, so it is likely they are also sdB+WD systems.

5.3. The minimum companion masses

To get a clearer picture of the masses of the close companions to hot subdwarf stars, we update the plot of RV semi-amplitude versus orbital period for all known sdB binaries (as shown in Kupfer et al. 2015) with spectroscopic solutions and with *TESS* or Kepler light curves (Fig. 18) as well as plot the minimum companion mass distribution in Fig. 19.

Our new sample adds many more systems with companion mass constraints to this plot. As we have seen, it is possible to constrain the minimum mass of the companion from the RV semi-amplitude of the sdB and the orbital period, when assuming a mass for the sdB. This is given by the black lines for different periods. For a random distribution of system angles, the probability to have a system with inclination $> 60^\circ$ is the same as

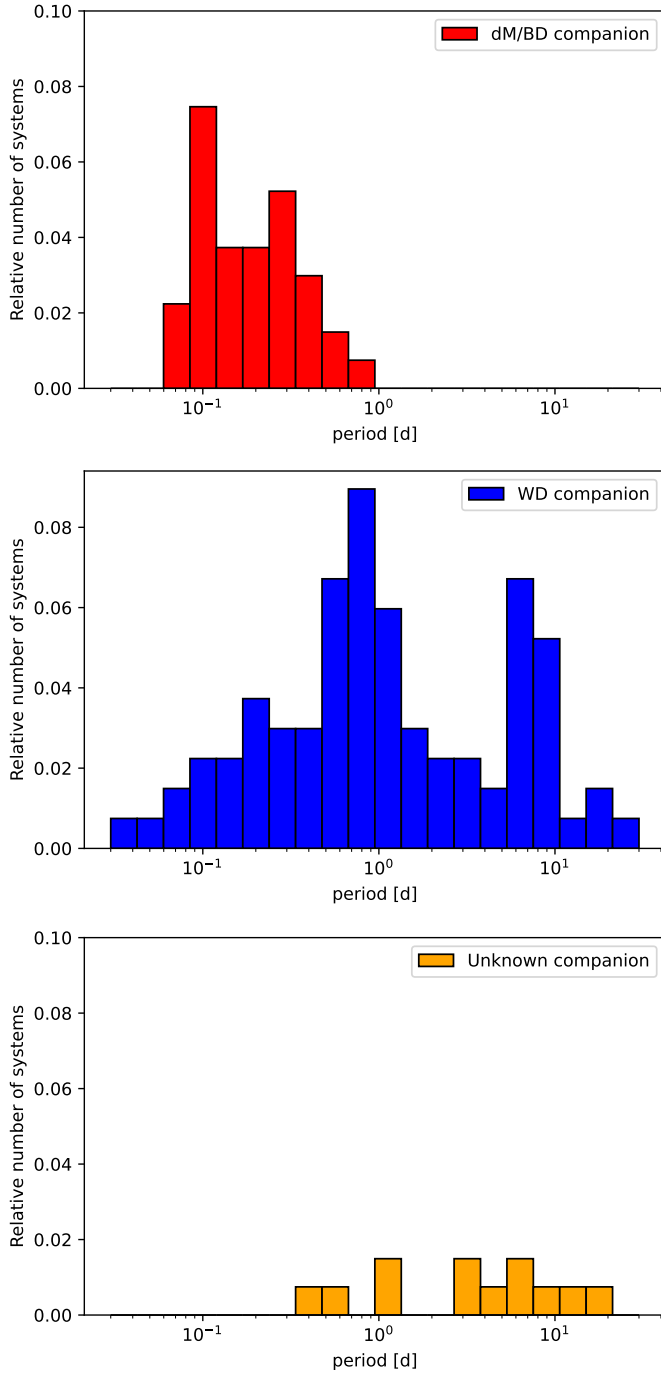


Fig. 17: Period distribution of the hot subdwarf binaries with solved orbits with dM/BD companions in the top panel, with WD companions in the middle and unknown companions in the lower panel.

for an inclination of $< 60^\circ$, and so about half of the companions should have masses of only up to 20% higher than the minimum companion mass.

We find that systems with cool, low-mass companions cluster around the hydrogen-burning limit with masses up to $0.25 M_\odot$ with one exception. The white dwarf companions to sdB stars have higher minimum masses, and it looks like there are three different populations. At the shortest periods from approximately one to about three hours, a small group of WD companions with minimum companion masses around 0.7 to $0.8 M_\odot$ are

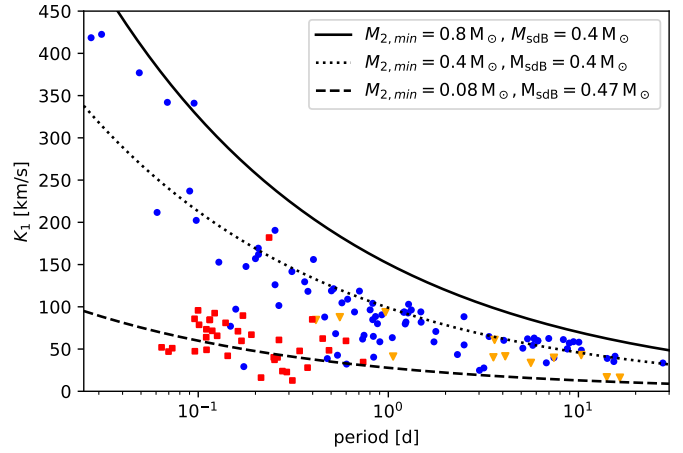


Fig. 18: RV semi-amplitudes of all known short-period sdB binaries with spectroscopic solutions and with *TESS* or Kepler light curves plotted against their orbital periods (red squares: dM/BD companions, blue circles: WD companions, yellow diamonds: unknown type). The lines mark a certain minimum companion mass derived from the binary mass function (assuming 0.47 or $0.4 M_\odot$ for the sdBs).

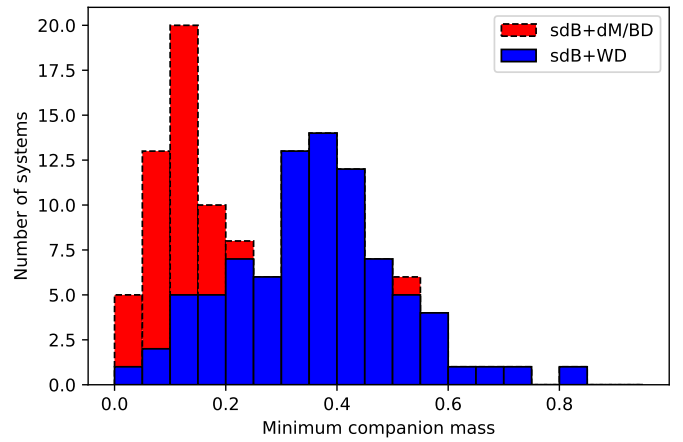


Fig. 19: Minimum companion mass distribution of all known short-period sdB binaries with spectroscopic solutions and with *TESS* or *K2* light curves (assuming $0.47 M_\odot$ for a sdB with dM/BD companion or $0.4 M_\odot$ for a sdB with WD companion).

found. Most of the WD companions are found in binaries with longer periods. Up to a period of about 4 days they seem to have significantly lower minimum companion masses with a mass ratio close to one (around $0.4 M_\odot$, when assuming an sdB mass of $0.4 M_\odot$). Systems with periods belonging to the second peak in the period distribution around 5–10 days show some indication of slightly higher minimum companion masses above $0.4 M_\odot$ up to $0.6 M_\odot$.

6. Discussion and Conclusions

Our light variation search increases the number of known reflection effect systems from 19 to 104 systems. Moreover, we detected 23 new sdB+WD systems showing tiny variations with amplitudes below $\sim 0.1\%$, due to Doppler beaming or ellipsoidal deformation in their light curves.

Table 2: Masses of the solved sdB+WD systems derived by light curve analysis and SED fitting

target	$M_{\text{sdB,SED}}$ [M_{\odot}]	$M_{\text{sdB,lc}}$ [M_{\odot}]	references
KPD1946+4340	$0.452^{+0.065}_{-0.056}$	$0.47^{+0.03}_{-0.03}$	Bloemen et al. (2011)
CD-3011223	$0.44^{+0.061}_{-0.056}$	$0.47^{+0.03}_{-0.03}$	Geier et al. (2013)
PTF1J0823+0819	$0.48^{+0.09}_{-0.08}$	$0.45^{+0.09}_{-0.07}$	Kupfer et al. (2017b)
EVR-CB-001	$0.294^{+0.04}_{-0.034}$	$0.21^{+0.05}_{-0.05}$	Ratzloff et al. (2019)
EVR-CB-004	$0.461^{+0.104}_{-0.082}$	$0.52^{+0.04}_{-0.04}$	Ratzloff et al. (2020b)
ZTFJ2130+4420	$0.378^{+0.061}_{-0.053}$	$0.337^{+0.015}_{-0.015}$	Kupfer et al. (2020b)
HD265435	$0.59^{+0.17}_{-0.14}$	$0.64^{+0.10}_{-0.09}$	Pelisoli et al. (2021)

The characterization of the reflection effect systems in our sample shows that all except one have hot subdwarf primaries. The one exception was a system with a white dwarf primary. Similar results were found in other surveys, such as EREBOS (Schaffenroth et al. 2019). The detection of a white dwarf primary is not a complete surprise since we selected targets from the *Gaia* DR2 catalogue of hot subluminous stars, which does have some overlap with the white dwarf catalogue. Nonetheless, most of the primaries in our systems should be sdO/B stars. The reflection effect is only visible in hot white dwarfs, which are much rarer. Moreover, white dwarfs are much fainter than hot subdwarf stars. And since sdBs are mainly formed by binary evolution, the binarity rate of sdBs is much higher than of WDs. That is why reflection effect systems with hot subdwarf primaries will dominate all surveys for reflection effect systems.

To check the mass determination of the sdB using the SED and the *Gaia* parallaxes, we compared the masses derived by this method with the masses derived by the light curve analysis of several ellipsoidal systems. This is shown in Table 2. The masses derived by the two different methods agree very well within the errors for all systems, thereby showing the validity of our spectrophotometric *Gaia* distance method.

The comparison of the mass distribution of the sdB+dM and the sdB+WD (Fig. 12) shows that they differ significantly. The mass distribution of sdBs with WD companions is shifted to lower masses compared to sdBs with dM/BD companions. This implies that sdBs with dM/BD companions come from a different population than sdBs with WD companions. The sdB+dM systems show a peak around the canonical mass for He burning and a few systems at higher and lower mass, as predicted by binary population synthesis models (Han et al. 2002, 2003). Those non-canonical systems can originate from young, higher-mass systems igniting He in the core under non-degenerate conditions or be pre-He WDs not massive enough for He-burning that are passing through the sdB region in the HRD. The sdB+WDs, on the other hand, show many more low-mass systems. The sdB binaries with massive companions are observed towards the Galactic plane, where younger stars are found. This indicates that those systems are preferably formed in younger populations than the sdB+dM stars. The other sdB+WD systems seem to be equally distributed on the sky (see Fig. 7).

The observation of space-based, high S/N light curves covering a time span of at least 27 days up to several months of so many sdBs gave us for the first time a large sample of reflection effect binaries. Since they were selected mainly from the *Gaia* hot subdwarf catalogue and had no prior RV measurements, this gives us the first period distribution of sdB+dM systems selected only by light variations. The orbital period distribution of post-CE binaries is mainly dependent on the criterion for the ejection

of the CE (Han et al. 2002), and so this distribution can be used to constrain the common-envelope phase when combined with the companion mass distribution as done in Ge et al. (2022) for the sample of hot subdwarf binaries from Kupfer et al. (2015) or comparing it to a modelled sdB binary sample using binary population synthesis.

Aided by high-quality *TESS* light curves, we could constrain the nature of the companion in 75% of the sdB binaries with solved orbits and compare them. As seen in Fig. 17, the period distribution of the sdB+dM systems is concentrated in a much smaller period range compared to the sdB+WD systems, which are found over a wide range of periods from 0.03–30 days. The distribution of the minimum companion masses found at a certain orbital period (Fig. 18) shows that the companions in the reflection effect systems have minimum masses typical for BD/dM systems ($0.05 - 0.2 M_{\odot}$). There is no change with the orbital period visible. For the sdB+WD systems this is different. There seem to be two distinct groups of companion masses. At the shortest periods below 0.1 d, WD companions with high minimum masses around $0.8 M_{\odot}$ are found, which could be CO or ONe WDs. At longer periods, the WD companions seem to have significantly lower minimum masses, with masses around $0.4 M_{\odot}$. Many of those could be He-WD companions. At the longest periods the masses seem to be slightly higher indicating a third population of low-mass CO WD companions. This could suggest that sdB+WD systems at the shortest periods come from a different population with higher-mass progenitors having higher-mass companions than the longer period sdB+WD systems, which is consistent with predictions by binary population synthesis (Han et al. 2002, 2003).

The high signal-to-noise light curves allowed us to derive parameters for a large number of sdB+dM/BD and sdB+WD systems. Details of this light curve modeling and analysis are discussed in a separate paper (Paper II).

As *TESS* continues to observe, the number of high-quality reflection effect and sdB+WD light curves will continue to grow. This will further increase our sample size and improve constraints on the mass and period distributions. Future spectroscopic and photometric surveys like 4MOST, BlackgGem, and Vera Rubin Observatory will also increase our sample size and our knowledge about these systems.

Acknowledgements. This research made use of Lightkurve, a Python package for Kepler and *TESS* data analysis (Lightkurve Collaboration et al. 2018). This paper includes data collected by the *TESS* mission, which are publicly available from the Mikulski Archive for Space Telescopes (MAST). Funding for the *TESS* mission is provided by NASA’s Science Mission directorate. VS and SG acknowledge funding from the German Academic Exchange Service (DAAD PPP USA 57444366) for this project and would like to thank the host institution Texas Tech University for the hospitality. VS was funded by the Deutsche Forschungsgemeinschaft under grant GE2506/9-1. IP was partially funded by the Deutsche Forschungsgemeinschaft under grant GE2506/12-1 and by the UK’s Science and Technology Facilities Council (STFC), grant ST/T000406/1. TK acknowledges support from the National Science Foundation through grant AST #2107982, from NASA through grant 80NSSC22K0338 and from STScI through grant HST-GO-16659.002-A. BNB was supported by the National Science Foundation grant AST-1812874. We thank Uli Heber for comments on the manuscript. We thank Andreas Irrgang for the development of the SED fitting tool and making it available to us.

References

- Afşar, M. & İbanoğlu, C. 2008, MNRAS, 391, 802
- Althaus, L. G., Miller Bertolami, M. M., & Córscico, A. H. 2013, A&A, 557, A19
- Astropy Collaboration, Price-Whelan, A. M., Sipőcz, B. M., et al. 2018, AJ, 156, 123
- Astropy Collaboration, Robitaille, T. P., Tollerud, E. J., et al. 2013, A&A, 558, A33

- Baran, A. S., Østensen, R. H., Heber, U., et al. 2021a, MNRAS, 503, 2157
 Baran, A. S., Sahoo, S. K., Sanjayan, S., & Ostrowski, J. 2021b, MNRAS
 Barlow, B. N., Corcoran, K. A., Parker, I. M., et al. 2022, ApJ, 928, 20
 Barlow, B. N., Kilkenny, D., Drechsel, H., et al. 2013, MNRAS, 430, 22
 Bell, K. J., Kosakowski, A., Kilic, M., et al. 2019, Research Notes of the American Astronomical Society, 3, 81
 Bloemen, S., Marsh, T. R., Østensen, R. H., et al. 2011, MNRAS, 410, 1787
 Brown, W. R., Beers, T. C., Wilhelm, R., et al. 2008, AJ, 135, 564
 Capitanio, L., Lallement, R., Vergely, J. L., Elyajouri, M., & Montreal-Ibero, A. 2017, A&A, 606, A65
 Chen, A., O'Donoghue, D., Stobie, R. S., et al. 1995, MNRAS, 275, 100
 Copperwheat, C. M., Morales-Rueda, L., Marsh, T. R., Maxted, P. F. L., & Heber, U. 2011, MNRAS, 415, 1381
 Dorman, B., Rood, R. T., & O'Connell, R. W. 1993, ApJ, 419, 596
 Drechsel, H., Heber, U., Napiwotzki, R., et al. 2001, A&A, 379, 893
 Drilling, J. S. 1985, ApJ, 294, L107
 Edelmann, H., Heber, U., Altmann, M., Karl, C., & Lisker, T. 2005, A&A, 442, 1023
 Edelmann, H., Heber, U., Hagen, H. J., et al. 2003, A&A, 400, 939
 For, B. Q., Green, E. M., Fontaine, G., et al. 2010, ApJ, 708, 253
 Gaia Collaboration, Brown, A. G. A., Vallenari, A., et al. 2018, A&A, 616, A1
 Gaia Collaboration, Brown, A. G. A., Vallenari, A., et al. 2021, A&A, 649, A1
 Ge, H., Tout, C. A., Chen, X., et al. 2022, arXiv e-prints, arXiv:2205.14256
 Geier, S. 2020, A&A, 635, A193
 Geier, S., Heber, U., Kupfer, T., & Napiwotzki, R. 2010, A&A, 515, A37
 Geier, S., Hirsch, H., Tillich, A., et al. 2011a, A&A, 530, A28
 Geier, S., Marsh, T. R., Wang, B., et al. 2013, A&A, 554, A54
 Geier, S., Napiwotzki, R., Heber, U., & Nelemans, G. 2011b, A&A, 528, L16
 Geier, S., Østensen, R. H., Heber, U., et al. 2014, A&A, 562, A95
 Geier, S., Østensen, R. H., Nemeth, P., et al. 2017, A&A, 600, A50
 Geier, S., Raddi, R., Gentile Fusillo, N. P., & Marsh, T. R. 2019, A&A, 621, A38
 Gray, D. F. 2005, The Observation and Analysis of Stellar Photospheres
 Han, Z., Podsiadlowski, P., Maxted, P. F. L., & Marsh, T. R. 2003, MNRAS, 341, 669
 Han, Z., Podsiadlowski, P., Maxted, P. F. L., Marsh, T. R., & Ivanova, N. 2002, MNRAS, 336, 449
 Heber, U. 2009, ARA&A, 47, 211
 Heber, U. 2016, PASP, 128, 082001
 Heber, U., Drechsel, H., Østensen, R., et al. 2004, A&A, 420, 251
 Heber, U., Irrgang, A., & Schaffenroth, J. 2018, Open Astronomy, 27, 35
 Hillwig, T. C., Frew, D. J., Reindl, N., et al. 2017, AJ, 153, 24
 Howell, S. B., Sobeck, C., Haas, M., et al. 2014, PASP, 126, 398
 Irrgang, A., Geier, S., Heber, U., et al. 2021, A&A, 650, A102
 Ivanova, N., Justham, S., Chen, X., et al. 2013, A&A Rev., 21, 59
 Jeffery, C. S. & Ramsay, G. 2014, MNRAS, 442, L61
 Kawka, A., Vennes, S., Németh, P., Kraus, M., & Kubát, J. 2010, MNRAS, 408, 992
 Kawka, A., Vennes, S., O'Toole, S., et al. 2015, MNRAS, 450, 3514
 Kilkenny, D., Koen, C., & Worters, H. 2010, MNRAS, 404, 376
 Kilkenny, D., O'Donoghue, D., Worters, H. L., et al. 2015, MNRAS, 453, 1879
 Kilkenny, D. & Stone, L. E. 1988, MNRAS, 234, 1011
 Kilkenny, D., Worters, H. L., O'Donoghue, D., et al. 2016, MNRAS, 459, 4343
 Koen, C. 2009, MNRAS, 395, 979
 Koen, C., O'Donoghue, D., Kilkenny, D., Stobie, R. S., & Saffer, R. A. 1999, MNRAS, 306, 213
 Krzesinski, J. & Balona, L. A. 2022, arXiv e-prints, arXiv:2204.01604
 Kupfer, T., Bauer, E. B., Burdge, K. B., et al. 2019, ApJ, 878, L35
 Kupfer, T., Bauer, E. B., Burdge, K. B., et al. 2020a, ApJ, 898, L25
 Kupfer, T., Bauer, E. B., Marsh, T. R., et al. 2020b, ApJ, 891, 45
 Kupfer, T., Bauer, E. B., van Roestel, J., et al. 2022, ApJ, 925, L12
 Kupfer, T., Geier, S., Heber, U., et al. 2015, A&A, 576, A44
 Kupfer, T., Ramsay, G., van Roestel, J., et al. 2017a, ApJ, 851, 28
 Kupfer, T., van Roestel, J., Brooks, J., et al. 2017b, ApJ, 835, 131
 Lallement, R., Vergely, J.-L., Valette, B., et al. 2014, A&A, 561, A91
 Lamontagne, R., Demers, S., Wesemael, F., Fontaine, G., & Irwin, M. J. 2000, AJ, 119, 241
 Latour, M., Fontaine, G., & Green, E. 2014, in Astronomical Society of the Pacific Conference Series, Vol. 481, 6th Meeting on Hot Subdwarf Stars and Related Objects, ed. V. van Grootel, E. Green, G. Fontaine, & S. Charpinet, 91
 Lei, Z., Zhao, J., Németh, P., & Zhao, G. 2018, ApJ, 868, 70
 Lightkurve Collaboration, Cardoso, J. V. d. M., Hedges, C., et al. 2018, Lightkurve: Kepler and TESS time series analysis in Python, Astrophysics Source Code Library
 Lomb, N. R. 1976, Ap&SS, 39, 447
 Lynas-Gray, A. E. 2021, Frontiers in Astronomy and Space Sciences, 8, 19
 Maxted, P. F. L., Heber, U., Marsh, T. R., & North, R. C. 2001, MNRAS, 326, 1391
 Menzies, J. W. & Marang, F. 1986, in IAU Symposium, Vol. 118, Instrumentation and Research Programmes for Small Telescopes, ed. J. B. Hearnshaw & P. L. Cottrell, 305
 Mickaelian, A. M. 2008, AJ, 136, 946
 Möller, L. 2021
 Morales-Rueda, L., Maxted, P. F. L., Marsh, T. R., Kilkenny, D., & O'Donoghue, D. 2005, in Astronomical Society of the Pacific Conference Series, Vol. 334, 14th European Workshop on White Dwarfs, ed. D. Koester & S. Moehler, 333
 Németh, P., Kawka, A., & Vennes, S. 2012, MNRAS, 427, 2180
 O'Donoghue, D., Kilkenny, D., Koen, C., et al. 2013, MNRAS, 431, 240
 Orosz, J. A. & Wade, R. A. 1999, MNRAS, 310, 773
 Østensen, R. H., Geier, S., Schaffenroth, V., et al. 2013, A&A, 559, A35
 Østensen, R. H., Green, E. M., Bloemen, S., et al. 2010a, MNRAS, 408, L51
 Østensen, R. H., Green, E. M., Bloemen, S., et al. 2010b, MNRAS, 408, L51
 Østensen, R. H., Oreiro, R., Solheim, J. E., et al. 2010c, A&A, 513, A6
 Pawar, T. 2020
 Pelisoli, I., Neunteufel, P., Geier, S., et al. 2021, Nature Astronomy, 5, 1052
 Pelisoli, I., Vos, J., Geier, S., Schaffenroth, V., & Baran, A. S. 2020, A&A, 642, A180
 Penoyre, Z., Belokurov, V., & Evans, N. W. 2022, MNRAS, 513, 2437
 Pribulla, T., Dimitrov, D., Kjurkchieva, D., et al. 2013, Information Bulletin on Variable Stars, 6067, 1
 Ratzloff, J. K., Barlow, B. N., Kupfer, T., et al. 2019, ApJ, 883, 51
 Ratzloff, J. K., Barlow, B. N., Németh, P., et al. 2020a, ApJ, 890, 126
 Ratzloff, J. K., Kupfer, T., Barlow, B. N., et al. 2020b, ApJ, 902, 92
 Reed, M. D., Kawaler, S. D., Zola, S., et al. 2004, MNRAS, 348, 1164
 Reed, M. D., Yeager, M., Vos, J., et al. 2020, MNRAS, 492, 5202
 Ricker, G. R., Winn, J. N., Vanderspek, R., et al. 2015, Journal of Astronomical Telescopes, Instruments, and Systems, 1, 014003
 Rodríguez-López, C., Ulla, A., & Garrido, R. 2007, MNRAS, 379, 1123
 Sahoo, S. K., Baran, A. S., Sanjayan, S., & Ostrowski, J. 2020, MNRAS, 499, 5508
 Scargle, J. D. 1982, ApJ, 263, 835
 Schaffenroth, V., Barlow, B. N., Geier, S., et al. 2019, A&A, 630, A80
 Schaffenroth, V., Casewell, S. L., Schneider, D., et al. 2021, MNRAS, 501, 3847
 Schaffenroth, V., Classen, L., Nagel, K., et al. 2014a, A&A, 570, A70
 Schaffenroth, V., Geier, S., Drechsel, H., et al. 2013, A&A, 553, A18
 Schaffenroth, V., Geier, S., Heber, U., et al. 2018, A&A, 614, A77
 Schaffenroth, V., Geier, S., Heber, U., et al. 2014b, A&A, 564, A98
 Schindewolf, M., Levitan, D., Heber, U., et al. 2015, A&A, 580, A117
 Silvotti, R., Østensen, R. H., Bloemen, S., et al. 2012, MNRAS, 424, 1752
 Vos, J., Németh, P., Vučković, M., Østensen, R., & Parsons, S. 2018, MNRAS, 473, 693
 Vučković, M., Aerts, C., Østensen, R., et al. 2007, A&A, 471, 605
 Vučković, M., Bloemen, S., & Østensen, R. 2014, in Astronomical Society of the Pacific Conference Series, Vol. 481, 6th Meeting on Hot Subdwarf Stars and Related Objects, ed. V. van Grootel, E. Green, G. Fontaine, & S. Charpinet, 259
 Vučković, M., Østensen, R. H., Aerts, C., et al. 2009, A&A, 505, 239
 Vučković, M., Østensen, R. H., Németh, P., Bloemen, S., & Pápics, P. I. 2016, A&A, 586, A146

Appendix A: Parameters of the close sdB binaries in TESS

Table A.1: Atmospheric and absolute parameters of the sdB binaries with spectroscopic parameters and with space-based light curves determined by spectroscopy and spectral energy distribution fitting together with the *Gaia* parallax.

target	$T_{\text{eff,spec}}$ [K]	$\log g_{\text{spec}}$ [cgs]	$T_{\text{eff,sed}}$ [K]	M_{sed} [M $_{\odot}$]	L_{sed} [L $_{\odot}$]	R_{sed} [R $_{\odot}$]
Reflection effect systems						
KPD2215+5037	29600 ± 1000	5.64 ± 0.10	27000^{+7000}_{-6000}	$0.445^{+0.063}_{-0.055}$	$19.9^{+1.9}_{-1.7}$	$0.170^{+0.005}_{-0.005}$
JL82	26500 ± 500	5.22 ± 0.1	26000^{+500}_{-600}	$0.294^{+0.04}_{-0.034}$	$21^{+1.9}_{-2.0}$	$0.222^{+0.006}_{-0.006}$
HE0230-4323	31552 ± 500	5.60 ± 0.07	34000^{+8000}_{-5000}	$0.635^{+0.118}_{-0.094}$	40^{+6}_{-5}	$0.211^{+0.014}_{-0.012}$
V1405Ori	35100 ± 800	5.66 ± 0.11	27000^{+2300}_{-2700}	$0.44^{+0.06}_{-0.055}$	36^{+5}_{-5}	$0.166^{+0.006}_{-0.006}$
Feige48	29850 ± 500	5.46 ± 0.05	28500^{+2500}_{-1800}	$0.47^{+0.064}_{-0.059}$	$32.2^{+3}_{-2.8}$	$0.213^{+0.007}_{-0.007}$
GALEXJ2205-3141	28150 ± 500	5.68 ± 0.10	26800^{+1100}_{-1000}	$0.597^{+0.078}_{-0.074}$	20.9^{+20}_{-18}	$0.186^{+0.005}_{-0.005}$
PHL457	26500 ± 1100	5.38 ± 0.12	24600^{+1200}_{-700}	$0.316^{+0.048}_{-0.042}$	$16.1^{+1.8}_{-1.8}$	$0.191^{+0.008}_{-0.008}$
KBS13	29700 ± 500	5.70 ± 0.05	-	$0.472^{+0.062}_{-0.057}$	$18.2^{+1.6}_{-1.5}$	$0.162^{+0.004}_{-0.004}$
CPD-64481	27500 ± 500	5.60 ± 0.05	26500^{+1200}_{-500}	$0.437^{+0.057}_{-0.050}$	$15.7^{+1.3}_{-1.3}$	$0.1748^{+0.0032}_{-0.0030}$
GALEXJ0321+4727	27990 ± 400	5.34 ± 0.07	-	$0.571^{+0.145}_{-0.112}$	36^{+8}_{-7}	$0.219^{+0.005}_{-0.004}$
J012022+395059	29400 ± 500	5.48 ± 0.05	26500^{+2100}_{-2100}	$0.561^{+0.136}_{-0.103}$	24^{+6}_{-4}	$0.194^{+0.019}_{-0.016}$
PG1329+159	29100 ± 900	5.62 ± 0.10	27400^{+1100}_{-1000}	$0.694^{+0.101}_{-0.088}$	$29.8^{+3.1}_{-2.9}$	$0.215^{+0.008}_{-0.008}$
BPSCS22169-0001	39300 ± 500	5.600 ± 0.05	40000^{+9000}_{-5000}	$0.584^{+0.091}_{-0.076}$	87^{+9}_{-8}	$0.202^{+0.009}_{-0.008}$
HS2333+3927	36500 ± 1000	5.70 ± 0.10	-	$0.578^{+0.094}_{-0.088}$	51^{+7}_{-6}	$0.177^{+0.011}_{-0.010}$
UVEX0328+5035	$28500 \pm (500)$	$5.500 \pm (0.05)$	-	$0.375^{+0.052}_{-0.046}$	$19.6^{+1.9}_{-1.8}$	$0.182^{+0.006}_{-0.006}$
PG1017-086	30300 ± 500	5.61 ± 0.10	-	$0.547^{+0.168}_{-0.126}$	28^{+8}_{-6}	$0.196^{+0.025}_{-0.021}$
EQ Psc	28700 ± 500	5.63 ± 0.05	25400^{+1300}_{-1300}	$0.353^{+0.048}_{-0.044}$	$13.2^{+1.3}_{-1.2}$	$0.151^{+0.005}_{-0.005}$
HE1318-2111	36300 ± 1000	5.42 ± 0.1	41000^{+6000}_{-5000}	$0.365^{+0.064}_{-0.055}$	60^{+8}_{-8}	$0.196^{+0.012}_{-0.011}$
GALEXJ09348-2512 ^a	40800 ± 500	5.55 ± 0.05	33000^{+12000}_{-6000}	$0.737^{+0.176}_{-0.143}$	133^{+30}_{-26}	$0.241^{+0.023}_{-0.020}$
EC01578-1743 ^a	32200 ± 500	5.75 ± 0.05	30000^{+3600}_{-2400}	$0.445^{+0.062}_{-0.053}$	$21.2^{+1.9}_{-1.7}$	$0.148^{+0.005}_{-0.004}$
TYC5977-517-1 ^a	35200 ± 500	5.69 ± 0.05	-	$0.462^{+0.07}_{-0.065}$	35^{+4}_{-4}	$0.162^{+0.08}_{-0.007}$
HW Vir systems						
AADor	42000 ± 1000	5.460 ± 0.05	35700^{+2800}_{-2200}	$0.464^{+0.058}_{-0.052}$	118^{+8}_{-8}	$0.206^{+0.005}_{-0.005}$
ATLASJ340	40000 ± 1000	5.450 ± 0.05	-	$0.510^{+0.098}_{-0.078}$	116^{+16}_{-14}	$0.225^{+0.014}_{-0.013}$
ATLASJ283	50000 ± 1000	5.600 ± 0.05	-	$0.511^{+0.075}_{-0.064}$	201^{+17}_{-16}	$0.189^{+0.008}_{-0.007}$
2M1533+3759	29200 ± 500	5.58 ± 0.05	-	$0.427^{+0.058}_{-0.053}$	$20.3^{+2.0}_{-1.8}$	$0.176^{+0.006}_{-0.005}$
ASAS102322-3737	28400 ± 500	5.600 ± 0.05	27900^{+4400}_{-2800}	$0.469^{+0.065}_{-0.056}$	$19.1^{+1.9}_{-1.6}$	$0.181^{+0.006}_{-0.005}$
2M1938+4603	29600 ± 500	5.43 ± 0.05	-	$0.441^{+0.058}_{-0.052}$	$31.6^{+2.7}_{-2.5}$	$0.213^{+0.006}_{-0.005}$
BULSC16335	31500 ± 500	5.70 ± 0.05	-	$0.437^{+0.121}_{-0.094}$	21^{+6}_{-5}	$0.156^{+0.018}_{-0.016}$
EC10246-2707	28900 ± 500	5.64 ± 0.05	26700^{+2900}_{-2600}	$0.500^{+0.076}_{-0.067}$	$19.8^{+2.3}_{-2.0}$	$0.178^{+0.008}_{-0.007}$
HWVir	28500 ± 500	5.63 ± 0.05	25700^{+1900}_{-1700}	$0.42^{+0.055}_{-0.050}$	$19.9^{+1.9}_{-1.7}$	$0.190^{+0.005}_{-0.005}$
HS2231+2441	28400 ± 500	5.39 ± 0.05	28800^{+2000}_{-1500}	$0.312^{+0.052}_{-0.043}$	$20.6^{+2.6}_{-2.3}$	$0.189^{+0.010}_{-0.009}$
PG1336-018	32800 ± 500	5.76 ± 0.05	34000^{+6000}_{-4000}	$0.480^{+0.070}_{-0.057}$	$22.9^{+2.3}_{-2.0}$	$0.153^{+0.005}_{-0.005}$
J082053+000843	25800 ± 300	5.52 ± 0.04	27600^{+1400}_{-1200}	$0.513^{+0.103}_{-0.082}$	$17.1^{+3.0}_{-2.5}$	$0.208^{+0.017}_{-0.015}$
HS0705+6700	28800 ± 900	5.40 ± 0.10	28000^{+2600}_{-2200}	$0.467^{+0.075}_{-0.063}$	31^{+4}_{-4}	$0.225^{+0.011}_{-0.010}$
J162256+473051	29000 ± 600	5.65 ± 0.06	28800^{+2800}_{-2000}	$0.308^{+0.076}_{-0.057}$	$12.1^{+2.7}_{-2.0}$	$0.139^{+0.014}_{-0.011}$
ATLASJ296	25000 ± 500	5.45 ± 0.05	19300^{+2000}_{-1500}	$0.399^{+0.075}_{-0.062}$	$13.8^{+2.2}_{-1.9}$	$0.199^{+0.013}_{-0.012}$
J192059+372220	27500 ± 1000	5.40 ± 0.10	-	$0.476^{+0.091}_{-0.076}$	27^{+5}_{-4}	$0.230^{+0.016}_{-0.014}$
V2008-1753	32800 ± 250	5.83 ± 0.04	-	$0.47^{+0.395}_{-0.179}$	14^{+13}_{-6}	$0.124^{+0.042}_{-0.026}$
NSVS14256825	40000 ± 500	5.50 ± 0.05	-	$0.406^{+0.059}_{-0.052}$	82^{+7}_{-8}	$0.189^{+0.007}_{-0.007}$
Ellipsoidal and beaming systems						
KPD1946+4340	34200 ± 500	5.43 ± 0.10	-	$0.452^{+0.065}_{-0.056}$	61^{+6}_{-5}	$0.216^{+0.008}_{-0.007}$
GD687	24300 ± 500	5.32 ± 0.07	27000^{+1800}_{-1700}	$0.283^{+0.042}_{-0.037}$	$11.7^{+1.5}_{-1.3}$	$0.194^{+0.008}_{-0.008}$
PG0941+280	29400 ± 500	5.43 ± 0.05	30000^{+270}_{-2000}	$0.363^{+0.053}_{-0.048}$	$25.1^{+2.7}_{-2.5}$	$0.194^{+0.008}_{-0.007}$
EVR-CB-004	41000 ± 200	4.55 ± 0.03	40000^{+5300}_{-2800}	$0.461^{+0.104}_{-0.082}$	910^{+190}_{-160}	$0.60^{+0.06}_{-0.05}$
GALEXJ0751+0925	30620 ± 400	5.74 ± 0.10	34000^{+8000}_{-6000}	$0.368^{+0.05}_{-0.046}$	$14.6^{+1.4}_{-1.3}$	$0.136^{+0.005}_{-0.004}$
PG1043+760	27600 ± 800	5.39 ± 0.10	28000^{+2100}_{-4000}	$0.289^{+0.038}_{-0.036}$	$17^{+1.6}_{-1.6}$	$0.180^{+0.005}_{-0.005}$
EVR-CB-001	18500 ± 500	4.96 ± 0.04	19900^{+2900}_{-2200}	$0.294^{+0.04}_{-0.034}$	$9.4^{+1.2}_{-1.1}$	$0.300^{+0.007}_{-0.007}$
KPD0422+5421	25000 ± 1500	5.40 ± 0.10	23100^{+1900}_{-1700}	$0.366^{+0.048}_{-0.044}$	$14.1^{+1.4}_{-1.3}$	$0.201^{+0.005}_{-0.005}$
HD265435	34300 ± 400	5.62 ± 0.10	26900^{+3900}_{-1300}	$0.59^{+0.17}_{-0.14}$	51^{+5}_{-5}	$0.203^{+0.007}_{-0.007}$
CD-3011223	29200 ± 400	5.66 ± 0.05	29000^{+4400}_{-2700}	$0.44^{+0.061}_{-0.056}$	$17.7^{+1.7}_{-1.6}$	$0.164^{+0.005}_{-0.005}$

ZTFJ2130+4420	42000 ± 300	5.77 ± 0.05	-	$0.378^{+0.061}_{-0.053}$	49^{+8}_{-7}	$0.134^{+0.007}_{-0.007}$
J113840-003531	31200 ± 600	5.54 ± 0.09	28500^{+3300}_{-1200}	$0.501^{+0.096}_{-0.078}$	34^{+6}_{-5}	$0.201^{+0.013}_{-0.013}$
KIC6614501	23700 ± 500	5.70 ± 0.10	-	$0.361^{+0.058}_{-0.049}$	$5.7^{+0.8}_{-0.7}$	$0.142^{+0.007}_{-0.007}$
UV01735+22	38000 ± 500	5.54 ± 0.05	36000^{+16000}_{-7000}	$0.48^{+0.07}_{-0.061}$	72^{+10}_{-9}	$0.197^{+0.008}_{-0.008}$
PG1232-136	26900 ± 500	5.71 ± 0.05	27000^{+1400}_{-1400}	$0.402^{+0.052}_{-0.049}$	$10.2^{+1.0}_{-0.9}$	$0.148^{+0.004}_{-0.004}$
PG0101+039	27500 ± 500	5.53 ± 0.07	26800^{+600}_{-700}	$0.409^{+0.053}_{-0.050}$	$17.2^{+1.6}_{-1.5}$	$0.183^{+0.005}_{-0.005}$
GALEXJ234947.7+384440	23800 ± 350	5.380 ± 0.06	$-^{+}_{-}$	$0.38^{+0.05}_{-0.05}$	$12.7^{+1.2}_{-1.2}$	$0.210^{+0.004}_{-0.004}$
PG1512+244	29900 ± 900	5.74 ± 0.09	27700^{+1300}_{-1200}	$0.41^{+0.06}_{-0.05}$	$14.7^{+1.3}_{-1.2}$	$0.143^{+0.004}_{-0.004}$
PG1519+640	30600 ± 500	5.72 ± 0.05	27600^{+2000}_{-900}	$0.45^{+0.06}_{-0.06}$	$18.6^{+1.6}_{-1.5}$	$0.154^{+0.004}_{-0.004}$
GALEXJ025023.8-040611	28300 ± 500	5.67 ± 0.10	27000^{+2300}_{-2300}	$0.47^{+0.07}_{-0.06}$	$16.5^{+1.7}_{-1.5}$	$0.166^{+0.006}_{-0.006}$
PG1743+477	27600 ± 800	5.57 ± 0.10	28000^{+1100}_{-1500}	$0.49^{+0.07}_{-0.06}$	$19.3^{+1.8}_{-1.7}$	$0.193^{+0.005}_{-0.005}$
PG1648+536	$31400 \pm (500)$	$5.62 \pm (0.05)$	$-^{+}_{-}$	$0.46^{+0.07}_{-0.06}$	$16.9^{+2.4}_{-2.2}$	$0.176^{+0.005}_{-0.005}$
PG1000+408	36400 ± 900	5.540 ± 0.10	38000^{+2300}_{-1700}	$0.65^{+0.11}_{-0.09}$	82^{+10}_{-9}	$0.229^{+0.011}_{-0.011}$
TONS183	27600 ± 0.05	5.43 ± 0.05	26170^{+270}_{-250}	$0.38^{+0.06}_{-0.05}$	$20.5^{+2.1}_{-1.9}$	$0.198^{+0.007}_{-0.007}$
GALEXJ225444.1-551505	31070 ± 300	5.80 ± 0.05	30700^{+1200}_{-900}	$0.39^{+0.06}_{-0.05}$	$14.4^{+1.2}_{-1.1}$	$0.131^{+0.0029}_{-0.0025}$
PG0133+114	29600 ± 900	5.66 ± 0.10	23700^{+1000}_{-800}	$0.38^{+0.06}_{-0.05}$	$15.9^{+1.7}_{-1.5}$	$0.152^{+0.006}_{-0.005}$
PG0934+186	35800 ± 200	5.65 ± 0.02	31300^{+3900}_{-1900}	$0.47^{+0.08}_{-0.06}$	43^{+5}_{-4}	$0.171^{+0.007}_{-0.007}$
CD-24731	35400 ± 500	5.90 ± 0.05	33500^{+1000}_{-500}	$0.36^{+0.08}_{-0.05}$	$18^{+1.3}_{-1.2}$	$0.1128^{+0.0022}_{-0.0021}$
PHL1539	35400 ± 500	5.500 ± 0.05	36000^{+10000}_{-5000}	$0.28^{+0.05}_{-0.04}$	34^{+4}_{-4}	$0.156^{+0.007}_{-0.007}$
PTF1J082340.04+081936.5	27000 ± 500	5.50 ± 0.05	26400^{+1200}_{-1200}	$0.48^{+0.09}_{-0.08}$	$20.1^{+3.3}_{-2.6}$	$0.205^{+0.013}_{-0.012}$

Notes: spectroscopic parameters can be found in [Kupfer et al. \(2015\)](#) and references therein as well as references in Table A.4

^a paper II

Table A.2: Atmospheric parameters, luminosities and radii of the reflection effect candidates without known atmospheric parameters determined by SED fitting and *Gaia* parallax.

target	$T_{\text{eff,sed}}$ [K]	$\log g_{\text{sed,canonical}}$ [cgs]	L_{sed} [L_{\odot}]	R_{sed} [R_{\odot}]
2M0748+3042	33700 ⁺⁴⁴⁰⁰ ₋₂₉₀₀	5.78	21 ⁺¹⁴ ₋₉	0.150 ^{+0.012} _{-0.015}
HE0505-3833	26500 ⁺¹⁴⁰⁰ ₋₁₃₀₀	5.63	13.2 ^{+3.1} _{-2.6}	0.175 ^{+0.008} _{-0.007}
MCT0049-3059	24300 ⁺⁷⁰⁰ ₋₅₀₀	5.43	15.3 ^{+2.2} _{-1.8}	0.221 ^{+0.010} _{-0.010}
TYC4542-482-1	16400 ⁺⁷⁹⁰⁰ ₋₂₄₀₀	5.15	8.7 ^{+2.6} _{-0.165}	0.305 ^{+0.028} _{-0.052}
EC21390-2930	29000 ⁺¹²⁰⁰⁰ ₋₅₀₀₀	5.38	17 ⁺⁴⁷ ₋₁₄	0.241 ^{+0.026} _{-0.049}
2MASSJ18424506+6956202	37000 ⁺¹²⁰⁰⁰ ₋₉₀₀₀	5.7	17 ⁺⁶⁷ ₋₁₇	0.169 ^{+0.032} _{-0.030}
GALEXJ06206-5705	31000 ⁺⁷⁰⁰⁰ ₋₅₀₀₀	5.65	16.7 ^{+20.3} _{-9.75}	0.176 ^{+0.017} _{-0.024}
2MASSJ06125523+5750507	27000 ⁺⁵⁰⁰⁰ ₋₄₀₀₀	5.59	10.3 ^{+13.1} _{-6.0}	0.185 ^{+0.026} _{-0.023}
EC01578-1743	30000 ⁺³⁷⁰⁰ ₋₂₄₀₀	5.73	14.9 ^{+8.6} _{-5.2}	0.158 ^{+0.009} _{-0.013}
KUV04421+1416	25700 ⁺²²⁰⁰ ₋₂₆₀₀	5.52	14 ⁺⁶ ₋₆	0.196 ^{+0.013} _{-0.011}
GALEXJ01077-6707	25200 ⁺¹²⁰⁰ ₋₁₂₀₀	5.48	15.3 ^{+3.3} _{-2.8}	0.208 ^{+0.008} _{-0.007}
GAIADR2 2333936291513550336	26300 ⁺²⁰⁰⁰ ₋₁₉₀₀	5.55	15 ⁺⁹ ₋₆	0.107 ^{+0.03} _{-0.025}
GAIADR2 3573130082641947392	25700 ⁺¹⁰⁰⁰ ₋₁₀₀₀	5.45	18.2 ^{+3.5} _{-2.8}	0.218 ^{+0.017} _{-0.011}
GAIADR2 6366169442902410368	25000 ⁺¹³⁰⁰ ₋₁₄₀₀	5.4	18 ⁺⁵ ₋₄	0.231 ^{+0.011} _{-0.011}
GAIADR2 6724092123091015552	29600 ⁺⁴⁵⁰⁰ ₋₂₈₀₀	5.35	33 ⁺²⁵ ₋₁₅	0.248 ^{+0.016} _{-0.025}
GAIADR2-2911497105202950400	27100 ⁺²⁷⁰⁰ ₋₂₂₀₀	5.52	17 ⁺⁹ ₋₆	0.2 ^{+0.016} _{-0.016}
GAIADR2-3040772322279673472	26700 ⁺¹²⁰⁰ ₋₁₁₀₀	5.3	29 ⁺⁷ ₋₆	0.256 ^{+0.013} _{-0.013}
GAIADR2-5434436383219257472	28300 ⁺³⁹⁰⁰ ₋₂₅₀₀	5.46	22 ⁺¹⁵ ₋₉	0.217 ^{+0.015} _{-0.02}
GaiaDR2-3040772322279673472	26600 ⁺¹⁴⁰⁰ ₋₁₃₀₀	5.30	28 ⁺⁸ ₋₆	0.256 ^{+0.014} _{-0.013}
GaiaDR2-2909497952544966272	29000 ⁺⁵⁰⁰⁰ ₋₄₀₀₀	5.68	13 ⁺¹³ ₋₇	0.17 ^{+0.014} _{-0.021}
GAIADR2 5416091856344970880	28300 ⁺³⁶⁰⁰ ₋₂₄₀₀	5.6	16 ⁺¹¹ ₋₇	0.184 ^{+0.016} _{-0.017}
GAIADR2 5576826952945841408	25800 ⁺²²⁰⁰ ₋₂₁₀₀	5.44	17 ⁺⁹ ₋₆	0.219 ^{+0.019} _{-0.017}
CRTSJ064417.6-464020	26800 ⁺³¹⁰⁰ ₋₂₄₀₀	5.42	20 ⁺¹² ₋₈	0.225 ^{+0.018} _{-0.018}
GAIADR2 5647303827227273088	42000 ⁺¹⁴⁰⁰⁰ ₋₅₀₀₀	5.7	60 ⁺¹⁰⁰ ₋₄₀	0.165 ^{+0.028} _{-0.023}
GAIADR2 5296462581763471104	36000 ⁺¹⁴⁰⁰⁰ ₋₆₀₀₀	5.82	16 ⁺⁴⁰ ₋₁₃	0.146 ^{+0.018} _{-0.027}
2MASSJ08412266+0630294	36700 ⁺³⁸⁰⁰ ₋₂₉₀₀	5.7	37 ⁺²¹ ₋₁₂	0.162 ^{+0.014} _{-0.013}
SDSSJ075314.03+111240.1	27800 ⁺²⁴⁰⁰ ₋₂₁₀₀	5.48	22 ⁺¹² ₋₈	0.212 ^{+0.026} _{-0.023}
GAIADR2 3083335826137398400	36000 ⁺¹¹⁰⁰⁰ ₋₇₀₀₀	5.9	15 ⁺³⁵ ₋₁₂	0.13 ^{+0.027} _{-0.023}
SDSSJ044246.86-071654.4	22700 ⁺¹¹⁰⁰ ₋₁₀₀₀	5.3	15.6 ^{+3.5} _{-2.9}	0.259 ^{+0.013} _{-0.012}
EC02406-6908	25100 ⁺²⁰⁰⁰ ₋₂₁₀₀	5.52	13 ⁺⁶ ₋₄	0.197 ^{+0.012} _{-0.011}
GALEXJ14019-7513	34000 ⁺¹⁴⁰⁰⁰ ₋₆₀₀₀	5.7	15 ⁺³⁹ ₋₁₂	0.16 ^{+0.017} _{-0.03}
HE0516-2311	25900 ⁺¹⁴⁰⁰ ₋₁₅₀₀	5.4	21 ⁺⁷ ₋₆	0.229 ^{+0.024} _{-0.021}
EC23068-4801	29900 ⁺³²⁰⁰ ₋₂₂₀₀	5.73	15 ⁺⁸ ₋₅	0.157 ^{+0.014} _{-0.013}
GAIADR2-6652952415078798208	24100 ⁺⁵³⁰⁰ ₋₃₀₀₀	4.6	48 ⁺⁶⁰ ₋₂₉	0.48 ^{+0.06} _{-0.06}
CRTS-J120928.2-435809	26000 ⁺²⁶⁰⁰ ₋₂₃₀₀	5.4	19 ⁺¹¹ ₋₇	0.228 ^{+0.021} _{-0.02}
GAIADR2-2943004023214007424	26300 ⁺²⁴⁰⁰ ₋₂₂₀₀	5.46	18 ⁺⁹ ₋₆	0.214 ^{+0.086} _{-0.076}
GAIADR2-5289914135324381696	30000 ⁺⁴⁴⁰⁰ ₋₂₈₀₀	5.6	20 ⁺¹⁶ ₋₉	0.183 ^{+0.026} _{-0.022}
PG1628+181	26000 ⁺¹⁵⁰⁰ ₋₁₄₀₀	5.45	18 ⁺⁶ ₋₅	0.216 ^{+0.015} _{-0.014}
J306.3118+58.8522	25400 ⁺²⁵⁴⁰⁰ ₋₂₅₀₀	5.65	10 ⁺⁹ ₋₅	0.176 ^{+0.041} _{-0.03}
GaiaDR2-2993468995592753920	29700 ⁺⁴⁷⁰⁰ ₋₂₉₀₀	5.54	22 ⁺¹⁹ ₋₁₀	0.198 ^{+0.023} _{-0.022}
J084.4719-00.8239	28400 ⁺²¹⁰⁰ ₋₁₆₀₀	5.52	21 ⁺⁸ ₋₅	0.2 ^{+0.013} _{-0.012}
J129.0542-08.0399	26700 ⁺²⁴⁰⁰ ₋₂₁₀₀	5.37	23 ⁺¹³ ₋₈	0.237 ^{+0.031} _{-0.025}
GaiaDR2-2969438206889996160	27700 ⁺³⁸⁰⁰ ₋₂₅₀₀	5.3	29 ⁺²¹ ₋₁₂	0.262 ^{+0.019} _{-0.024}
J089.3714-14.1662	28000 ⁺⁶⁰⁰⁰ ₋₄₀₀₀	5.52	16 ⁺¹⁸ ₋₉	0.203 ^{+0.019} _{-0.025}

Table A.3: Classification of *TESS* targets with no variations

target	period	K_1	$M_{2,\min}(M_{\text{sdB}} = 0.47 M_{\odot})$	$M_{2,\min}(M_{\text{sdB}} = 0.4 M_{\odot})$	signal-to-noise
White dwarf companions (M dwarf excluded)					
KPD1930+2752	0.0950933	341	0.90	0.85	ell
J083006+475150	0.1478000000	77.00	0.14	0.12	1%
GALEXJ0805-1058	0.1737030000	29.20	0.05	0.04	0.04%
J165404+303701	0.2535700000	126.10	0.32	0.29	0.4%
HE0532-4503	0.2656000000	101.50	0.25	0.22	0.4%
KUV16256+4034	0.4776000000	38.70	0.10	0.09	0.02%
GALEXJ0507+0348	0.5281270000	68.20	0.20	0.18	0.2%
PG1247+554	0.60274	32.20	0.09	0.08	0.01%
PG1248+164	0.7323200000	61.80	0.20	0.18	0.5%
PG0849+319	0.7450700000	66.30	0.22	0.20	0.5%
PG1230+052	0.8371770000	40.40	0.13	0.11	0.1%
PG1116+301	0.8562100000	88.50	0.34	0.32	0.4%
PG0918+029	0.8767900000	80.00	0.30	0.28	0.1%
EC12408-1427	0.9024300000	58.60	0.20	0.19	0.05%
PG2331+038	1.2049640000	93.50	0.44	0.40	0.5%
HE1047-0436	1.2132500000	94.00	0.44	0.41	0.5%
HE2150-0238	1.3210000000	96.30	0.48	0.44	0.3%
PG1403+316	1.7384600000	58.50	0.27	0.25	0.7%
V1093Her	1.7773200000	70.80	0.35	0.33	0.3%
CPD-201123	2.3098	43.50	0.21	0.19	0.05%
TON245	2.5010000000	88.30	0.58	0.54	0.5%
PG1253+284	3.01634	24.80	0.12	0.11	0.01%
PG0958-073	3.1809500000	27.60	0.14	0.12	0.7%
KIC10553698	3.3870000000	64.80	0.42	0.39	lc
J183249+630910	5.4000000000	62.10	0.50	0.46	0.5%
HE1115-0631	5.8700000000	61.90	0.52	0.48	1%
PG0907+123	6.1163600000	59.80	0.51	0.47	0.2%
PG1032+406	6.7791000000	33.70	0.24	0.22	0.1%
Feige108	8.7465100000	50.20	0.46	0.43	0.5%
KIC11558725	10.0545000000	58.10	0.63	0.58	lc
KIC7668647	14.1742000000	38.90	0.40	0.37	lc
LB1516	10.3598000000	48.600	0.48	0.44	0.2%
PG1619+522	15.3578000000	35.20	0.36	0.33	0.1%
White dwarf companions (minimum mass, ^a Kupfer et al. (2015))					
J082332+113641	0.2070700000	169.40	0.44	0.41	3%
J172624+274419 ^a	0.5019800000	118.90	0.41	0.37	5%
KPD2040+3955	1.4828600000	94.00	0.49	0.45	3%
J002323-002953 ^a	1.4876000000	81.80	0.40	0.37	2%
GALEXJ0812+1601 ^a	5.1000000000	51.00	0.37	0.34	1%
PG1244+113 ^a	5.7521100000	54.40	0.43	0.39	1%
J095238+625818 ^a	6.9800000000	62.50	0.58	0.54	1%
PG0940+068	8.3300000000	61.20	0.62	0.57	0.3%
Feige108 ^a	8.7465100000	50.20	0.46	0.43	1%
EC20260-4757	8.9520000000	57.10	0.57	0.53	0.5%
PG1110+294 ^a	9.4152000000	58.70	0.61	0.57	1%
PG0919+273 ^a	15.5830000000	41.50	0.47	0.43	1%
PG0850+170	27.8150000000	33.50	0.45	0.42	0.1%
Undefined companions					
J095101+034757	0.4159000000	84.40	0.23	0.21	1.5%
HE1059-2735	0.5556240000	87.70	0.28	0.26	1%
J150829+494050	0.9671640000	93.60	0.39	0.36	1%
J113241-063652	1.0600000000	41.10	0.14	0.13	1.5%
KPD0025+5402	3.5711000000	40.20	0.23	0.21	3%
PB7352	3.6216600000	60.80	0.40	0.37	2%
TONS135	4.1228000000	41.40	0.25	0.23	0.5%
PG0839+399	5.6222000000	33.60	0.22	0.20	1%
J032138+053840	7.4327	39.70	0.31	0.28	0.3%
PG1558-007	10.3495000000	42.80	0.40	0.37	0.75%
CS1246	14.1050000000	16.60	0.13	0.12	3%
EGB5	16.5320000000	16.10	0.14	0.13	0.3%

Table A.4: All confirmed systems with light variations

TIC number	name	alternative name	RA [deg]	DEC [deg]	classification G [mag]	$B_p - R_p$ [mag]	parallax distance G_abs [pc]	period pm [mag]	reference ^a
reflection effect systems									
4491131	2M0748+3042	Tor287	117.233	30.713	sdB	14.046156 -0.347797	1.334	0.750	4.672 / 10.473
14081239	HE0505-3833	HE0505-3833a	76.745	-38.488	sdB	14.145108 -0.362259	1.228	0.815	4.591 / 8.454
28762714	FBS0145+363	"	36.564	-36.564	sdB	14.462710 -0.194446	3.786	8.354	12.404
66398320	MCT049-3059	PHL867	12.907	-30.716	sdB	14.340959 -0.392432	0.907	1.102	4.130 / 10.141
67423472	2M0156+4003	"	29.005	40.056	sDBVp	14.430020 -0.347691	3.438	0.291	4.111 / 8.833
103871878	2MASSJ2002943+3137190	"	300.123	31.622	sd	15.480430 0.090571	0.755	1.324	4.871 / 10.932
12288490	2MASSJ18330407+4637053	"	278.267	46.618	sDBV+dM	15.698741 -0.312881	1.433	0.698	6.481 / 11.739
137608661	2M0943+7831	TYC4544-2658-1	145.973	78.538	sDB	11.111541 -0.416957	3.899	0.256	4.066 / 8.485
138025887	2MASSJ0545291+7745425	"	88.72	77.762	sDB	15.808988 -0.040666	0.816	1.226	5.367 / 7.348
14278398	TYC4542-482-1	TYC4542-482-1	154.505	75.224	sd	12.597594 -0.237924	2.139	0.467	4.249 / 8.021
162128750	2MASSJ22035140+3002560	"	330.964	30.049	sd	13.595135 -0.286156	1.417	0.706	4.353 / 9.129
17329499	2MASSJ23063044+4418488	FBS2304+440	346.627	44.314	sd	14.289134 -0.127421	1.606	0.623	5.318 / 10.536
189585096	GALEXJ09348-2512	GALEXJ09348-251248	143.701	-25.213	sDB	13.044951 -0.422069	1.047	0.955	3.145 / 9.094
207085743	JL251	JL251	23.053	-49.561	sD	14.297598 -0.350369	0.950	1.053	4.186 / 9.246
209395544	EC21390-2930	TYC6952-17-1	325.487	-29.275	sDB+F	12.802671 -0.350422	1.677	0.596	3.926 / 10.106
229751806	2MASSJ18424506+6956202	HS1843+6953	280.688	69.939	sDB	15.237090 -0.344261	0.619	1.616	4.194 / 8.622
240946701	2MASSJ01135301+5001532	"	18.471	50.087	sd	14.954076 -0.093790	1.021	0.979	7.444 / 10.444
258826647	HS1909+7004	CRTSJ000231.3+425310	287.227	70.159	sDB	15.478670 -0.279844	0.416	2.403	3.575 / 3.862
259257018	2MASSJ00231294+4253099	"	0.63	42.886	sd	14.322986 -0.226666	0.926	1.080	4.156 / 6.193
260369118	GALEXJ06206-5705	95.161	-57.094	sD	14.669856 -0.341110	0.869	1.151	4.365 / 8.955	
270491267	2M1529-7011	2MASSJ15292631+701154370	232.36	70.198	sD	12.444365 -0.359034	1.981	0.505	3.929 / 5.543
279373920	TYC4470-864-1	TYC4470-864-1	324.573	72.186	sd	11.331290 -0.289723	1.460	0.685	2.152 / 5.231
312220636	2MASSJ05534886+3256017	2MASSJ05534886+3256017	88.454	32.934	sDB	14.134800 -0.058189	1.460	0.685	4.956 / 8.035
322550178	2MASSJ06125523+5750507	"	93.23	57.848	sd	15.785784 -0.236645	0.609	1.641	4.710 / 8.712
333419799	2MASSJ23354250+3944269	HS2333+3927	353.927	39.741	sDB+dM	14.565003 -0.288533	0.848	1.179	4.207 / 7.031
409644971	GALEXJ175340.57-500741.80	"	268.419	-50.128	sDB+F7V	12.893204 0.441393	1.249	0.801	3.375 / 8.460
422761655	EC01578-1743	GD1068	30.055	-17.479	sDB	12.023732 -0.364106	3.510	0.285	4.750 / 10.262
436579904	KUV04421+1416	KUV04421+1416	71.237	14.364	sDBVp	14.947878 0.367522	1.441	0.694	5.742 / 9.106
466277784	GALEXJ20228-6525	"	305.713	-65.423	sDB	13.283805 -0.320836	1.662	0.602	4.387 / 9.105
52078744	GALEXJ01077-6707	"	16.941	-67.128	sDB	13.915939 -0.254942	1.397	0.716	4.642 / 10.325
1672501769	GAIAADR2 52.664688020206471296	"	97.502	-71.894	sd	14.247365 -0.24032	1.089	0.919	4.432 / 8.590
268722844	GAIAADR2 22.086788999172871424	"	347.643	65.009	sd	14.590969 0.117362	1.366	0.732	5.268 / 9.915
2714949927	WISEJ003429.04+73329	GAIADR2 53.704092828447632	8.621	73.558	sd	14.594332 0.087897	1.293	0.773	5.153 / 8.538
272025132	LAMOSTJ001655-34+511349.7	GAIADR2 39499124.522199040	51.230	42.230	sd	16.327900 -0.195572	0.468	2.136	4.680 / 10.442
122884940	GAIADR2 2118607522015143936	"	46.618	278.267	sd	15.698741 -0.312881	1.433	0.698	6.481 / 11.739
360026652	J194649.77+395957.3	GAIADR2 2073337845177375488	39.994	39.994	sd	14.381372 -0.156038	0.836	1.196	3.993 / 10.387
96951246	J074.5734+30.5930	GAIADR2 15695941997427456	74.574	30.593	sd	16.701506 0.311461	0.951	1.052	5.592 / 10.930
202836039	GAIADR2 391484413605892096	"	8.422	49.670	sd	16.094654 -0.179928	0.511	1.958	4.635 / 8.911
367014246	J077.5424+30.1127	GAIADR2 156174219292762624	77.542	30.113	sd	15.741088 0.230362	0.869	1.150	5.437 / 7.727
295895179	J304.2697+53.7150	GAIADR2 2184734315978100096	53.715	53.715	sd	16.325259 0.030304	0.635	1.574	5.340 / 9.917
5051080	TYC5977-517-1	"	109.919	-21.889	sDB	12.131400 -0.357847	2.822	0.354	4.384 / 9.293
12379252	GAIADR2 2333936291513550336	TonS138	001.290	-26.530	sDB	15.990884 -0.372682	0.461	2.168	4.311 / 7.843
386644511	GAIADR2 3573130082641947392	PG1145-135	177.050	-13.772	sd	14.255842 -0.338502	0.986	1.014	4.225 / 9.982
2652124418	GAIADR2 63.66169442902410368	IL24	293.905	-76.804	sDB	15.260036 0.011102	0.798	1.253	4.771 / 10.978
86141703	GAIADR2 67.24092123091015552	"	271.718	-43.559	sd	13.453639 -0.198243	1.300	0.769	4.023 / 10.064
37004041	GAIADR2 2911497105202950400	"	090.1499	-25.198	sd	15.138751 -0.341063	0.674	1.483	4.783 / 8.304
63113578	GAIADR2 2921050693020996864	"	104.606	-25.415	sd	11.4817005 0.229303	2.693	0.371	3.638 / 5.793
32302937	GAIADR2 3040772322279673472	"	117.391	-09.096	sd	14.247949 -0.293413	0.849	1.177	3.893 / 7.644
73238638	GAIADR2 3083216116810048768	J08032076-0039394	-80.661	-76.804	sd	15.407982 -0.367592	0.471	2.121	4.675 / 10.930
170310610	GAIADR2 54.3443638219257472	"	151.133	-35.062	sd	14.031923 -0.268618	1.100	0.909	4.239 / 9.303
775878600	GAIADR2 55.6199385810491264	"	102.726	-44.265	sd	15.302058 -0.260799	1.035	0.966	5.375 / 12.533
1036707852	GAIADR2 58.7853036051735424	"	218.251	-61.355	sd	15.063677 0.222188	1.478	0.676	5.912 / 9.258
4161582	GAIADR2 88025005422941440	LA MOSTI073756.25+311646.5	114.484	+31.280	sDB	13.553999 -0.257770	1.289	0.776	4.105 / 10.202
406417817	GAIADR2 1831343410431617920	"	308.210	+24.193	sd	14.702023 -0.069664	0.885	1.129	4.438 / 10.087

397532904	GAIAADR2 2303705631625361024	"	12.870154 0.105246 0.902	1.109	2.646	5.258	10.09	Baran et al. (2021b)	
609725827	GAIAADR2 564551735705888384	"	16.536114 -0.166992 0.384	2.603	4.458	9.264	2.56	Baran et al. (2021b)	
17391	GAIAADR2 304072322279673472	"	14.271790 -0.361527 1.161	1.177	3.893	7.644	6.28	Geier et al. (2019)	
900666	GAIAADR2 3090497955254966272	"	15.541340 -0.244382 0.614	1.629	4.482	8.979	6.42	Geier et al. (2019)	
112588	GAIAADR2 30618984417753216	"	16.373169 0.431673 0.570	1.753	5.154	5.948	3.98	Geier et al. (2019)	
83081722	GAIAADR2 5526271511387514880	"	15.532911 -0.21985 0.659	1.57	4.628	11.581	2.51	Geier et al. (2019)	
10132341	GAIAADR2 541609185634490880	"	16.240723 -0.030918 0.438	2.281	4.450	6.879	4.96	Geier et al. (2019)	
108121382	GAIAADR2 5611820525418506608	"	15.921090 0.197431 0.470	1.215	4.284	8.431	3.40	Geier et al. (2019)	
123027362	GAIAADR2 5511191365810066176	"	13.890878 -0.204649 1.398	0.715	4.618	10.701	2.52	Geier et al. (2019)	
146117756	GAIAADR2 554653351352096192	"	15.530023 0.306595 0.544	1.837	4.409	9.772	7.44	Geier et al. (2019)	
148044670	GAIAADR2 5576826955941408	"	15.046183 -0.206454 0.764	1.309	4.461	9.405	3.05	Geier et al. (2019)	
154909544	GAIAADR2 556111050498563	"	15.329434 -0.272529 0.605	1.652	4.239	8.497	7.60	Geier et al. (2019)	
170100070	CRTSII084417.6-464020	"	15.968775 -0.116289 0.628	1.593	4.958	9.033	3.16	Geier et al. (2019)	
270808951	GAIAADR2 5511191365810066176	"	16.046017 -0.367107 0.376	2.663	3.919	9.716	2.87	Geier et al. (2019)	
123417	GAIAADR2 554653351352096192	"	16.200662 -0.106041 0.576	1.735	5.004	10.256	6.34	Geier et al. (2019)	
122670	GAIAADR2 556111050498563	"	16.415363 0.181255 0.864	1.157	6.099	9.875	25.1	Geier et al. (2019)	
101074	GAIAADR2 556111050498563	"	14.809977 -0.375967 0.758	1.319	4.209	7.325	8.08	Geier et al. (2019)	
105150	+06.940	"	14.370837 0.233464	1.042	0.960	4.460	9.811	5.8	Geier et al. (2019)
111946	-28.373	"	15.15763 -0.150249 0.719	1.391	4.436	7.943	2.67	Geier et al. (2019)	
113398	-33.947	"	13.484192 -0.405651 1.100	0.909	3.692	6.267	5.16	Geier et al. (2019)	
122231	-38.416	"	16.200662 -0.106041 0.576	1.735	5.004	10.256	6.34	Geier et al. (2019)	
122670	-29.364	"	16.415363 0.181255 0.864	1.157	6.099	9.875	25.1	Geier et al. (2019)	
101074	-46.672	"	14.809977 -0.375967 0.758	1.319	4.209	7.325	8.08	Geier et al. (2019)	
105150	+06.940	"	14.370837 0.233464	1.042	0.960	4.460	9.811	5.8	Geier et al. (2019)
111946	-46.672	"	15.15763 -0.150249 0.719	1.391	4.436	7.943	2.67	Geier et al. (2019)	
113398	-65.037	"	13.484192 -0.405651 1.100	0.909	3.692	6.267	5.16	Geier et al. (2019)	
122231	-10.765	"	15.327970 -0.061670 0.732	1.366	4.651	8.282	32.95	Geier et al. (2019)	
122670	-29.364	"	15.587963 -0.346142 0.479	2.088	3.990	8.708	6.39	Geier et al. (2019)	
101074	+06.508	"	16.227335 -0.399355 0.469	1.440	4.125	8.549	6.35	Geier et al. (2019)	
105150	-69.641	"	15.465370 -0.196526 0.875	1.143	4.274	9.502	2.67	Geier et al. (2019)	
111946	-23.896	"	15.900676 0.316098 0.622	1.608	4.270	6.454	4.98	Geier et al. (2019)	
113398	-65.037	"	15.189713 0.059291 0.771	1.297	4.626	10.357	3.09	Geier et al. (2019)	
122231	-16.268	"	15.327970 -0.061670 0.732	1.366	4.651	8.282	32.95	Geier et al. (2019)	
122670	+11.211	"	15.587963 -0.346142 0.479	2.088	3.990	8.708	6.39	Geier et al. (2019)	
101074	122435	"	16.227335 -0.399355 0.469	1.440	4.125	8.549	6.35	Geier et al. (2019)	
105150	-00.564	"	15.465370 -0.196526 0.875	1.143	4.274	9.502	2.67	Geier et al. (2019)	
111946	-07.282	"	15.900676 0.316098 0.622	1.608	4.270	6.454	4.98	Geier et al. (2019)	
113398	-41.986	"	15.189713 0.059291 0.771	1.297	4.626	10.357	3.09	Geier et al. (2019)	
122231	-19.528	"	15.327970 -0.061670 0.732	1.366	4.651	8.282	32.95	Geier et al. (2019)	
122670	-16.268	"	15.587963 -0.346142 0.479	2.088	3.990	8.708	6.39	Geier et al. (2019)	
101074	122435	"	16.227335 -0.399355 0.469	1.440	4.125	8.549	6.35	Geier et al. (2019)	
105150	-07.282	"	15.465370 -0.196526 0.875	1.143	4.274	9.502	2.67	Geier et al. (2019)	
111946	-41.986	"	15.900676 0.316098 0.622	1.608	4.270	6.454	4.98	Geier et al. (2019)	
113398	-65.037	"	15.189713 0.059291 0.771	1.297	4.626	10.357	3.09	Geier et al. (2019)	
122231	-27.972	"	15.327970 -0.061670 0.732	1.366	4.651	8.282	32.95	Geier et al. (2019)	
122670	-30.883	"	15.587963 -0.346142 0.479	2.088	3.990	8.708	6.39	Geier et al. (2019)	
101074	-72.81	"	16.2341767 -0.340793 2.273	0.440	4.125	9.306	17.6	Koen (2009)	
105150	-43.174	"	13.724080 0.331779 1.151	0.869	4.026	8.575	10.81	Kilkenny et al. (2010)	
111946	-07.282	"	14.948787 0.367522 1.441	0.694	5.742	9.106	9.55	Reed et al. (2020)	
113398	-41.986	"	13.414267 -0.401045 1.264	0.791	3.921	10.566	8.25	Reed et al. (2020)	
122231	-27.972	"	15.189713 0.059291 0.771	1.297	4.626	10.357	3.09	Geier et al. (2019)	
122670	-33.337	"	15.327970 -0.061670 0.732	1.366	4.651	8.282	32.95	Geier et al. (2019)	
101074	-34.001	"	12.341767 -0.340793 2.273	0.440	4.125	9.306	17.6	Koen (2009)	
105150	-34.174	"	13.724080 0.331779 1.151	0.869	4.026	8.575	10.81	Kilkenny et al. (2010)	
111946	-07.282	"	14.948787 0.367522 1.441	0.694	5.742	9.106	9.55	Reed et al. (2020)	
113398	-41.986	"	13.414267 -0.401045 1.264	0.791	3.921	10.566	8.25	Reed et al. (2020)	
122231	-27.972	"	15.189713 0.059291 0.771	1.297	4.626	10.357	3.09	Geier et al. (2019)	
122670	-33.337	"	15.327970 -0.061670 0.732	1.366	4.651	8.282	32.95	Geier et al. (2019)	
101074	-34.001	"	12.341767 -0.340793 2.273	0.440	4.125	9.306	17.6	Koen (2009)	
105150	-34.174	"	13.724080 0.331779 1.151	0.869	4.026	8.575	10.81	Kilkenny et al. (2010)	
111946	-07.282	"	14.948787 0.367522 1.441	0.694	5.742	9.106	9.55	Reed et al. (2020)	
113398	-41.986	"	13.414267 -0.401045 1.264	0.791	3.921	10.566	8.25	Reed et al. (2020)	
122231	-27.972	"	15.189713 0.059291 0.771	1.297	4.626	10.357	3.09	Geier et al. (2019)	
122670	-33.337	"	15.327970 -0.061670 0.732	1.366	4.651	8.282	32.95	Geier et al. (2019)	
101074	-34.001	"	12.341767 -0.340793 2.273	0.440	4.125	9.306	17.6	Koen (2009)	
105150	-34.174	"	13.724080 0.331779 1.151	0.869	4.026	8.575	10.81	Kilkenny et al. (2010)	
111946	-07.282	"	14.948787 0.367522 1.441	0.694	5.742	9.106	9.55	Reed et al. (2020)	
113398	-41.986	"	13.414267 -0.401045 1.264	0.791	3.921	10.566	8.25	Reed et al. (2020)	
122231	-27.972	"	15.189713 0.059291 0.771	1.297	4.626	10.357	3.09	Geier et al. (2019)	
122670	-33.337	"	15.327970 -0.061670 0.732	1.366	4.651	8.282	32.95	Geier et al. (2019)	
101074	-34.001	"	12.341767 -0.340793 2.273	0.440	4.125	9.306	17.6	Koen (2009)	
105150	-34.174	"	13.724080 0.331779 1.151	0.869	4.026	8.575	10.81	Kilkenny et al. (2010)	
111946	-07.282	"	14.948787 0.367522 1.441	0.694	5.742	9.106	9.55	Reed et al. (2020)	
113398	-41.986	"	13.414267 -0.401045 1.264	0.791	3.921	10.566	8.25	Reed et al. (2020)	
122231	-27.972	"	15.189713 0.059291 0.771	1.297	4.626	10.357	3.09	Geier et al. (2019)	
122670	-33.337	"	15.327970 -0.061670 0.732	1.366	4.651	8.282	32.95	Geier et al. (2019)	
101074	-34.001	"	12.341767 -0.340793 2.273	0.440	4.125	9.306	17.6	Koen (2009)	
105150	-34.174	"	13.724080 0.331779 1.151	0.869	4.026	8.575	10.81	Kilkenny et al. (2010)	
111946	-07.282	"	14.948787 0.367522 1.441	0.694	5.742	9.106	9.55	Reed et al. (2020)	
113398	-41.986	"	13.414267 -0.401045 1.264	0.791	3.921	10.566	8.25	Reed et al. (2020)	
122231	-27.972	"	15.189713 0.059291 0.771	1.297	4.626	10.357	3.09	Geier et al. (2019)	
122670	-33.337	"	15.327970 -0.061670 0.732	1.366	4.651	8.282	32.95	Geier et al. (2019)	
101074	-34.001	"	12.341767 -0.340793 2.273	0.440	4.125	9.306	17.6	Koen (2009)	
105150	-34.174	"	13.724080 0.331779 1.151	0.869	4.026	8.575	10.81	Kilkenny et al. (2010)	
111946	-07.282	"	14.948787 0.367522 1.441	0.694	5.742	9.106	9.55	Reed et al. (2020)	
113398	-41.986	"	13.414267 -0.401045 1.264	0.791	3.921	10.566	8.25	Reed et al. (2020)	
122231	-27.972	"	15.189713 0.059291 0.771	1.297	4.626	10.357	3.09	Geier et al. (2019)	
122670	-33.337	"	15.327970 -0.061670 0.732	1.366	4.651	8.282	32.95	Geier et al. (2019)	
101074	-34.001	"	12.341767 -0.340793 2.273	0.440	4.125	9.306	17.6	Koen (2009)	
105150	-34.174	"	13.724080 0.331779 1.151	0.869	4.026	8.575	10.81	Kilkenny et al. (2010)	
111946	-07.282	"	14.948787 0.367522 1.441	0.694	5.742	9.106	9.55	Reed et al. (2020)	
113398	-41.986	"	13.414267 -0.401045 1.264	0.791	3.921	10.566	8.25	Reed et al. (2020)	
122231	-27.972	"	15.189713 0.059291 0.771	1.297	4.626	10.357	3.09	Geier et al. (2019)	
122670	-33.337	"	15.327970 -0.061670 0.732	1.366	4.651	8.282	32.95	Geier et al. (2019)	
101074	-34.001	"	12.341767 -0.340793 2.273	0.440	4.125	9.306	17.6	Koen (2009)	
105150	-34.174	"	13.724080 0.331779 1.151	0.869	4.026	8.575	10.81	Kilkenny et al. (2010)	
111946	-07.282	"	14.948787 0.367522 1.441	0.694	5.742	9.106	9.55	Reed et al. (2020)	
113398	-41.986	"	13.414267 -0.401045 1.264	0.791	3.921	10.566	8.25	Reed et al. (2020)	
122231	-27.972	"	15.189713 0.059291 0.771	1.297	4.626	10.357	3.09	Geier et al. (2019)	
122670	-33.337	"	15.327970 -0.061670 0.732	1.366	4.651	8.282	32.95	Geier et al. (2019)	
101074	-34.001	"	12.341767 -0.340793 2.273	0.440	4.125	9.306	17.6	Koen (2009)	
105150	-34.174	"	13.724080 0.331779 1.151	0.869	4.026	8.575	10.81	Kilkenny et al. (2010)	
111946	-07.282	"	14.948787 0.367522 1.441	0.694	5.742	9.10			

Baran et al. (2021a)		Pribulla et al. (2013)		Schaffennroth et al. (2019)		
441613385	VSX1075328.9+722424	"		16.480227 -0.210146 0.376	2.662 4.354 9.295	
2003333263	J331.6658+32.7267	"	sdB	16.921835 -0.149397 0.304	3.287 4.338 9.566	
9440665036	J309.1155+23.8396	"	sd	16.967440 -0.073616 0.412	5.044 5.044 10.633	
76760933	GAIAADR2 6652952415078798208	"	sd	13.832330 -0.275429 0.529	1.890 2.450 8.786	
33743252	CRIS J120928.2538509	"	sd	13.536974 -0.197598 0.621	1.835 4.301 9.051	
42 4266802	GAIAADR2 2943004023214007424	"	sd	13.994193 -0.240567 1.198	4.387 7.755 11.73	
19 6239-02.8462	J096.6239-02.8462	"	sdB	16.0096 0.1308681 0.535	1.868 4.653 5.848	
308541002	GAIAADR2 5289914135324381696	"	sd	16.539120 -0.154041 0.420	2.379 4.657 12.216	
818308005	GAIAADR2 5518740367833012224	"	sd	17.446575 -0.012933 0.076	1.3141 1.853 10.763	
351628-1.81	PG1628-1.81	"	sdB	15.372973 -0.270555 0.628	1.591 4.364 9.654	
459182998	GAIAADR2 1131845039229607680	"	sd	16.141038 -0.322172 0.402	2.487 4.163 9.755	
1400704733	GAIAADR2 1417117518648285056	"	sd	16.999810 0.351522 0.292	3.419 4.330 10.760	
19 79105817	J129.3118+58.8522	"	sd	17.534945 0.132929 0.385	2.599 5.461 9.493	
2051607908	GAIAADR2 2283172389416472320	"	sd	17.622341 -0.023394 0.355	2.817 5.373 10.345	
1684897611	GAIAADR2 452743855589780352	"	sd	17.549710 -0.284513 0.191	5.249 3.949 10.911	
3426474736	GAIAADR2 299346899559273920	"	sd	15.907853 -0.074766 0.527	1.896 4.518 7.839	
13179405	J197.4719-00.8339	"	sd	15.181983 -0.070962 0.803	1.245 4.706 6.987	
51431668	J129.0542-08.399	"	sd	15.280132 -0.367052 0.507	1.972 3.805 6.859	
139397815	GAIAADR2 2969438206889996160	"	sdB	13.594079 -0.349399 1.077	0.929 3.754 6.130	
139785230	J112.2726-18.6176	"	sd	15.912261 0.193732 0.507	1.972 4.438 9.927	
3126749962	J109.7402+07.6536	"	sd	15.216421 -0.404513 0.525	1.906 3.816 5.843	
312171081	J080.5805+10.6719	"	sd	14.472228 0.258853 1.450	0.690 5.278 8.708	
317804295	J089.3714-14.1662	"	sd	15.924339 0.439569 0.977	0.103 5.874 8.410	
425064757	AA Dor	"	sdOB	11.099821 -0.478417 2.838	0.352 3.365 9.687	
2046417955	GAIAADR2 2003241230122936	ATLASJ340	sdB	14.979544 0.011270 0.701	1.427 4.208 6.789	
FFI	ATLASJ283	J283.0316+14.763		14.992987 0.239105 0.852	1.174 4.645 10.888	
		283.0316892389 +14.76306734.63 sdB		14.992987 0.239105 0.852	1.174 4.645 10.888	
148785530	2M1533+3759	FBS1531+381	sdB+dm	12.941533 -0.383593 1.905	0.525 4.340 9.108	
73704693	ASAS02322-3737	TYC7767-376-1	sdB+dm	11.692036 -0.3525816 3.543	0.282 4.439 9.625	
27 1164763	2M1938+4603	KIC9472174	sdB+dm	12.111415 -0.344645 2.441	0.410 4.052 6.288	
k2-c09	OGLE-BUL-SC 163335	OGLE-BLG-ECL-163	sdB+dm	16.544252 0.269485 0.668	1.496 5.670 6.869	
19 3092806	EC10246-2707	EC10246-2707	sdB+dm	14.473673 0.328232 1.018	0.982 4.477 6.714	
22 228755638	HWVir	"	sdB+dm	10.590979 -0.358919 0.573	0.173 4.397 6.892	
175402069	PG1336-018	NYVir	sdBVp+dm	13.366823 -0.401715 1.680	0.595 4.493 9.023	
611402948	J018.4128+22.9608	PTF1011339.09+225739.1	sd	16.610086 -0.386513 0.422	2.369 4.737 8.927	
FFI	PTF10724+1253	J111.232	+22.9608	sdB	17.8432 -0.477333 0.240	1.467 4.719 9.503
HS0705-6700	HS0705-6700	+12.8833		14.616244 -0.360858 0.789	1.267 4.103 9.054	
9941129	J08205+0008843.4	V470Cam	sdB+dm	14.518632 -0.351009 0.657	1.523 4.245 6.969	
455206965	J162256+473051	PG1621-476	sdB+dm	16.21870 -0.403603 0.551	1.814 4.926 9.412	
193555713	ATLASJ296	2MASSJ19444284+5449426	sdB	15.750846 -0.233982 0.644	1.552 4.797 7.874	
467187065				15.761664 -0.141020 0.498	2.007 4.249 8.415	
FFI	J192059+372220	SDSSJ192059.78+372220.0		15.761664 -0.141020 0.498	2.007 4.249 8.415	
		290.24904856394 +37.37221528999 sdB		15.761664 -0.141020 0.498	2.007 4.249 8.415	
		Ellipsoidal + beaming systems		15.761664 -0.141020 0.498	2.007 4.249 8.415	
272717401	KPD1946+4340	"	sdOB	14.223958 -0.278768 0.852	1.174 3.876 7.482	
67 598107	HD68783	296.9287	+43.7924	14.074328 -0.376294 1.205	0.830 4.479 9.878	
233635672	PG0941+280	-34.007	sdB	13.196795 -0.403038 1.532	0.653 4.122 11.372	
1973623	EVR-CB-004	145.977	+27.783	13.107076 -0.271864 0.422	2.367 1.236 5.097	
320417198	GALEXJ075147.0+092526	133.302	-28.768	14.064508 -0.382053 1.478	0.677 4.913 9.188	
142491300	PG1043+760	117.946	+09.424	13.701308 -0.328960 1.446	4.502 4.811 2.76	
FFI	EVR-CB-001	161.771	+75.740	12.566651 -0.155235 2.207	0.453 4.286 10.072	
8773089	KPD0422+5421	132.065	-74.322	14.626647 -0.220573 1.507	0.663 5.518 9.625	
68495594	HD265435	066.529	+54.471	12.087978 -0.425845 2.167	0.462 3.767 6.204	
		103.351	+33.059	-30.884 -0.387547 2.820	0.355 4.547 6.922	
		212.817		12.296123 -0.387547 2.820	0.355 4.547 6.922	
		322.736	+44.346	13.701308 -0.313504 1.088	1.309 4.854 6.422	
		-29.803		19.932531 -0.368810 2.214	0.528 6.300 12.251	
		035.583	-23.416	11.988973 -0.404593 3.108	0.322 4.452 9.598	
		103.351	-44.224	13.637440 -0.365522 1.527	0.655 4.556 10.650	
		174.669	-00.592	14.42396 -0.4355413 0.773	1.294 3.864 11.552	
		294.208	-42.0288	15.953427 -0.258789 0.792	1.262 5.430 6.052	
		188.828	-13.919	13.229093 -0.368810 2.214	0.452 4.955 11.597	
		146.360	-21.449	11.80116 -0.452111 2.281	0.438 3.592 8.045	
		203.923	-14.670	13.637440 -0.361939 1.580	0.633 4.359 9.698	
		265.829	+21.5438	13.9928 -0.266407 1.070	0.935 4.139 9.354	

45575305	GALEX1234947.7+384440	"	357.449	+38.745	sDB	11.715421	-0.189247	3.872	0.258	4.655	3.698	10.38	Kawka et al. (2010)
229664008	PG1512+244	"	228.635	+24.178	sDB	13.176018	-0.364226	2.170	0.461	4.858	11.138	30.48	Morales-Rueda et al. (2005)
137840206	EC2202-1834	"	335.742	-18.320	sDB	13.790620	-0.370770	1.195	0.837	4.177	10.120	16.92	Copperwheat et al. (2011)
22980551	EC21556.5552	"	329.753	-55.634	sDB	13.103904	-0.394528	2.022	0.495	4.632	6.748	20.89	Copperwheat et al. (2011)
202491630	PG1519+640	"	230.130	+63.869	sDB	12.379927	-0.423141	2.734	0.366	4.564	10.382	12.97	Copperwheat et al. (2011)
10932480	GALEX1025023.8-040611	"	042.600	-04.104	sDB	13.002628	-0.386107	2.025	0.494	4.535	10.632	15.92	Nemeth et al. (2012)
193600962	PG1743+477	"	266.110	+47.696	sDB	13.734726	-0.386953	1.293	0.773	4.293	9.162	12.03	Morales-Rueda et al. (2005)
274385041	PG1648+536	"	252.499	+53.525	sDB	14.009392	-0.338769	1.172	0.853	4.354	10.726	13.02	Copperwheat et al. (2011)
9376301	PG1000+408	"	150.976	+40.572	sDB	13.249913	-0.509614	0.999	1.001	3.248	9.690	26.76	Copperwheat et al. (2011)
66493797	TONS183	"	015.323	-33.713	sDB	12.581187	-0.410837	2.048	0.488	4.138	8.605	19.87	Geier et al. (2011a)
220488137	GALEX1225444.1-551505	"	343.686	-55.252	sDB	12.141099	-0.453345	3.384	0.296	4.788	9.584	29.25	Kawka et al. (2015)
346894954	PG0133+114	"	024.109	+11.659	sDB	12.275509	-0.344523	3.153	0.317	4.769	9.905	29.70	Morales-Rueda et al. (2005)
91986289	PG0934+186	"	144.318	+18.420	sDB	13.075914	-0.458850	1.538	0.650	4.010	9.247	97.73	Copperwheat et al. (2011)
33490778	CD-24731	"	025.952	-24.086	sDB	11.684070	-0.494827	4.334	0.231	4.869	11.611	138.74	Geier et al. (2011a)
142875987	PHL1539	"	051.643	-31.062	sDB	14.022624	-0.479381	1.076	0.930	4.181	10.142	60.11	Bell et al. (2019)
Central stars of planetary nebula													
342025025	UUSe	"	295.543	+17.0873	sD0	14.974704	0.284213	0.365	2.739	2.787	9.559	11.16	Afşar & İbanoğlu (2008)
423311936	V477Lyr	"	277.827	+26.937	sD0	14.957651	-0.229764	0.404	2.474	2.991	6.469	11.32	Afşar & İbanoğlu (2008)
FFI	HaTr7	"	268.539	-60.833	sD0	14.829035	-0.306667	0.587	3.672	10.279	7.73	Hillwig et al. (2017)	
334382552	EGB5	"	122.803	+10.955	sD0	13.775318	-0.472623	1.593	0.628	4.787	10.030	396.77	Geier et al. (2011b)
120596335	CD-486027	"	163.669	-48.785	sD0	12.135967	-0.276526	1.226	0.816	2.579	8.616	8.57	Drilling (1985)

^a light variation analysis and/or atmospheric parameters or spectral classification